OE Optical Engineering

TUTORIAL

# Communication performance in the focusing and saturation regimes inherent to the turbulent channel: a tutorial

**Larry B. Stotts[a,*] and Larry C. Andrews[b]**
[a]Resident Consultant, Science and Technology Associates, Fairfax Drive, Arlington, Virginia, United States
[b]Towns Laser Institute, Center for Research in Electro-Optics and Lasers, College of Optics, University of Central Florida, Orlando, Florida, United States

**ABSTRACT.** Early studies of laser beam propagating in turbulence indicated that the log-amplitude variance of the received intensity would grow without bound as the refractive index structure parameter and range increase. This was an ominous observation. It suggests that the laser communications and remote sensing systems would not be useful during the hot daytime conditions. Fortunately, it does not increase without limit. We describe the various scintillation indices that predict this type of performance. Specifically, we will develop the scintillation indices for satellite communications (SATCOM) downlink, SATCOM uplink, and atmospheric slant path and horizontal communications link geometries, which also include tracking, untracked, and aperture averaging receiver effects. The focusing and saturation regimes in the turbulent channel will be defined. An example analysis will be provided using this information. The importance of log-amplitude variance is that the scintillation indices will have peak values for some refractive index structure parameters and range values.

 [DOI: 10.1117/1.OE.63.12.120801]

**Keywords:** free-space optical communications; turbulence

Paper 20240910T received Sep. 11, 2024; revised Nov. 7, 2024; accepted Nov. 19, 2024; published Dec. 11, 2024.

## 1 Introduction

Free-space optical communication (FSOC) networks operating through, and within, the atmosphere require optical links to close under strong intensity fluctuations conditions in the turbulent channel to be useful.[1–8] These conditions usually occur during daytime operations. Early atmospheric communications link analyses only addressed signal degradation mitigation believing that one just needed more optical power to communicate at range. That is true, but that is not the total story. What was missing is that the turbulent-intensity noise variance really is the factor that affects communications performance, not just the turbulent Strehl ratios. Specifically, it helps define the received power via the turbulence-based power penalty[9] as well as quantifying the turbulent channel's intensity probability density functions (PDFs)[10–12] and the signal-to-noise ratio (SNR).[10–12] (Andrews and Phillips[10] recognized that the turbulent-based intensity variance adds to the system noise variance of the SNR) These entities are all key factors in calculating the system's bit error rate (BER) and probability of fading, major system performance parameters.[10–12] In short, it is the limiting factor on whether the system meets specifications or not.

*Address all correspondence to Larry B. Stotts, lbstotts@gmail.com

Scintillation refers to the temporal or spatial intensity fluctuations of an optical wave caused by small random refractive-index fluctuations. The parameter associated with these intensity fluctuations is the "scintillation index," which is defined as

$$\sigma_I^2(\mathrm{r}, L) = \frac{\langle I^2(\mathrm{r}, L)\rangle - \langle I(\mathrm{r}, L)\rangle^2}{\langle I(\mathrm{r}, L)\rangle^2} = \frac{\langle I^2(\mathrm{r}, L)\rangle}{\langle I(\mathrm{r}, L)\rangle^2} - 1, \tag{1}$$

where $\mathbf{r} = (x, y)$ is the transverse distance at the link range $L$, $I(\mathbf{r}, L)$ is received intensity at range, and the brackets $\langle \cdots \rangle$ denote an ensemble average. Using weak intensity fluctuation theory, many early investigations into the scintillation characteristics of an optical wave were concerned with the log-amplitude variance, which is written as

$$\sigma_\chi^2 = 0.307 C_n^2(h_0) k^{7/6} L^{11/6}, \tag{2}$$

where $C_n^2(h_0)$ is the "refractive index structure parameter," $h_0$ is the link altitude above ground level, $k = 2\pi/\lambda$ is the optical wave number, and $\lambda$ is the wavelength. Alternatively, some studies focused on the "log-intensity variance," $\sigma_{\ln I}^2 = 4\sigma_\chi^2$. The relationships between the scintillation index and these other parameters are

$$\sigma_I^2 = \exp(4\sigma_\chi^2) - 1 = \exp(\sigma_{\ln I}^2) - 1. \tag{3}$$

Under weak intensity fluctuations, we have the related expression

$$\sigma_I^2 \approx \sigma_{\ln I}^2. \tag{4}$$

Focusing on the log-amplitude variance, Eq. (2) appears to grow without bound as $C_n^2(h_0)$ and $L$ increase. This was an ominous observation. It suggested that the FSOC system would not be useful during the hot daytime conditions. Fortunately, $\sigma_\chi^2$ does not increase without limit. With increasing $C_n^2(h_0)$ and $L$, $\sigma_\chi$ (observed) reaches its peak value when $\sigma_\chi$ (Rytov theory) is roughly $\sigma_\chi \approx 0.3$, and then decreases slightly for increasing $\sigma_\chi$.[6–20] This effect is illustrated in Fig. 1, derived from a reported set of horizontal link measurements by Gracheva.[14] Near the Earth's surface, the horizontal path saturation of $\sigma_\chi^2$ for visible light occurs within a few hundred meters of the transmitter, as shown in Fig. 1. This asymptotic falloff regime for large values of $\sigma_\chi$ is called the saturation regime. Unfortunately, it took over 20 years to develop theories that cover all the reported experimental results.

Many of the early theoretical treatments of scintillation concentrated on simple field models such as an unbounded plane wave and spherical wave, or "point source." However, in many applications, the plane wave and spherical wave approximations are not sufficient to characterize the scintillation properties of the wave, particularly when focusing and finite beam characteristics are important. In such cases, the lowest-order Gaussian-beam wave model is more characteristic of a laser beam, limiting forms that lead to the plane wave and spherical wave models.

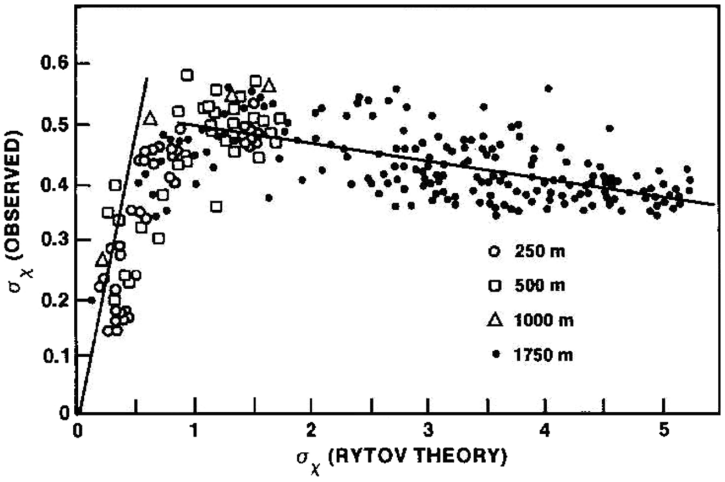


**Fig. 1** Observed log-amplitude variance versus predicted log-amplitude variance.

The governing integrals for the Gaussian-beam wave scintillation index under weak intensity fluctuations were developed in the mid-1960s and some analytical solutions were published based on the Kolmogorov spectrum.[15–17] However, tractable analytical formulations for the scintillation index of a Gaussian-beam wave in the receiver (Rx) pupil plane under general atmospheric conditions, including inner and outer scale effects, were not developed until much later.[18,19] The decrease in scintillation associated with increasing telescope aperture size had been recognized in early astronomical measurements made in the 1950s,[20] although analytic expressions for the aperture-averaged scintillation index with inner and outer scale in the detector plane of an Rx with aperture diameter $D_{Rx}$ were not developed until more recently.[21]

This paper is a tutorial describing the various scintillation index theories that predict the type of performance depicted in Fig. 1. Specifically, this paper will develop the scintillation indices for satellite communications (SATCOM) downlink, SATCOM uplink, and atmospheric slant path and horizontal communications link geometries, which also include tracking, untracked, and aperture averaging receiver effects. The focusing and saturation regimes in the turbulent channel will be defined. An example analysis will be provided using this information. The key aspect of this tutorial is that no matter whether the detection system is incoherent or coherent and/or which signaling format is used, the scintillation indices will have peak values for some particular $C_n^2(h_0)$ and range values. If the system specifications are not met, this analysis will show an example of other turbulence mitigation techniques that can be employed to get the desired system performance.

## 2 Kolmogorov Theory of Turbulence

Classical turbulence deals with the random velocity fluctuations of viscous fluid such as the atmosphere. Although the atmosphere has two distinct states of motion, laminar and turbulent flow, the latter is where dynamic mixing occurs, resulting in random sub-flows called turbulent eddies. The transition to this mixing state from laminar flow depends on the critical Reynolds number of the fluid derived from the flow characteristics. This parameter is non-dimensional and is denoted by $\mathrm{Re} = Vl/v$, where $V$ in meters per second (m/s) and $l$ in meters (m) are the velocity (speed) and "dimension" of the flow, respectively, and $v$ in meter-squared per second $(\mathrm{m}^2/\mathrm{s})$ is the kinematic viscosity. Near the ground, the critical Reynolds number is around $10^5$, which indicates that the motion is highly turbulent. This is a state that degrades optical laser beam propagation. The mathematical characterization of this state is derived from the non-linear Navier–Stokes equations. Because of the difficulty in solving these equations, Kolmogorov developed a statistical theory of turbulence that is based on one-dimensional analyses employing insightful simplifications and approximations. In short, the Kolmogorov turbulence theory is a set of hypotheses based heavily on physical insights, not solutions derived from the first principles.

His theory proposes that the small-scale structure of turbulence is statistically homogeneous, isotropic, and independent of the large-scale structure. To understand his structure of atmospheric turbulence, it is convenient to adopt a visualization tool named "the energy cascade theory" due to Richardson.[22] This tool is shown in Fig. 2. The source of energy at large scales is either wind shear or convection. When the wind speed is sufficiently high that the critical Reynolds number is exceeded, large unstable air masses (conceptualized as "eddies") are created with characteristic dimensions slightly smaller than, and independent of, the parent flow. Under the influence of inertial forces, the larger eddies break up into smaller eddies to form a continuum of eddy size for the transfer of energy from the macroscale $L_0$ (called the outer scale of turbulence) to the microscale $l_0$ (called the inner scale of turbulence). The family of eddies bound above by the outer scale $L_0$ and below by the inner scale $l_0$ forms the inertial subrange. Scale sizes smaller than the inner scale $l_0$ belong to the viscous dissipation range. In this last regime, the turbulent eddies disappear, and the remaining energy in the fluid motion is dissipated as heat.

The outer scale $L_0$ denotes the scale size below which turbule properties are independent of the parent flow. In the surface layer up to ~100 m, the outer scale $L_0$ is usually assumed to grow linearly with the order of the height of the above ground of the observation point (Ref. 10, p. 60). Eddies of scale size smaller than $L_0$ are assumed statistically homogeneous and isotropic, whereas those equal to or greater than $L_0$ are generally non-isotropic, and their structure is not

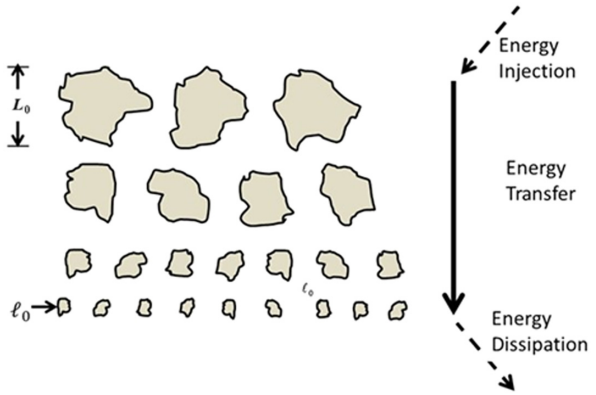


**Fig. 2** Kolmogorov cascade theory of turbulence, where $L_0$ denotes the outer scale of turbulence and $l_0$ denotes the inner scale of turbulence.

well defined. Above 100 m, the horizontal dimension of $L_0$ is generally much greater than its vertical dimension because of stratification. As the turbulent eddies become smaller and smaller, the relative amount of energy dissipated by viscous forces increases until the energy dissipated matches that supplied by the kinetic energy of the parent flow. When this happens, the Reynolds number is reduced to the order of unity, and the associated eddy size then defines the inner scale of turbulence $l_0$. The inner scale is typically on the order of 1 to 10 mm near the ground but is on the order of centimeters or more in the troposphere and stratosphere. On the other hand, for beams propagating near the ground, the outer scale $L_0$ is approximately half of the transmitter height above the ground. The outer scale can be tens of meters in the upper atmosphere.

## 3 Power Spectrum Models

To calculate the scintillation index, the three-dimensional spatial power spectrum of the atmospheric refractive index $\Phi_n(\boldsymbol{\kappa})$ needs to be known.[10] The power spectrum is the Fourier transform of the refractive index covariance function.[10] For completeness, the chronological list of power spectrum models used in the scintillation index and other turbulent parameter investigations will be presented in this section.

### 3.1 Kolmogorov Spectrum

To model atmospheric turbulence, we use power spectrum models of the refractive index. The most used model for optical/infrared wave propagation is the three-dimensional "Kolmogorov power-law spectrum"

$$\Phi_n(\kappa) = 0.033 C_n^2 \kappa^{-11/3}, \quad 1/L_0 \ll \kappa \ll 1/l_0, \tag{5}$$

where $\kappa = |\boldsymbol{\kappa}|$ is the atmospheric wave number or spatial frequency. Although this spectrum model is theoretically valid only over the spatial wavenumber inertial range $1/L_0 \ll \kappa \ll 1/l_0$, it is often extended over all wave numbers by assuming that the inner scale $l_0$ is negligibly small and the outer scale $L_0$ is infinite. However, this can often lead to integrals that do not converge, so caution is called for in extending this wavenumber domain.

Although many researchers rely on the Kolmogorov spectrum, which ignores inner and outer scale effects, we find that inner and outer scales can both play an important role in the analysis of the scintillation index.

### 3.2 Modified von Kármán Spectrum

The "modified von Kármán spectrum" is defined by

$$\Phi_n(\kappa) = 0.033 C_n^2 \frac{\exp(-\kappa^2/\kappa_m^2)}{(\kappa^2 + \kappa_0^2)^{11/6}}, \quad 0 \le \kappa < \infty \tag{6}$$

where $\kappa_m = 5.92/l_0$ and $\kappa_0 = 2\pi/L_0$. However, it is widely known that the outer scale has no effect on scintillation in the weak intensity fluctuation regime. It does begin to play a prominent

role in moderate-to-strong turbulence. This spectrum model with $\kappa_0 = 0$ leads to the "Tatarskii spectrum"

$$\Phi_n(\kappa) = 0.033 C_n^2 \kappa^{-11/3} \exp\left(-\frac{\kappa^2}{\kappa_m^2}\right), \quad \kappa \gg 1/L_0 \tag{7}$$

where $\kappa_m = 5.92/l_0$.

### 3.3 Modified Atmospheric Spectrum

Another spectrum model that includes both inner and outer scale parameters but also exhibits a high wave number rise (or "bump") just prior to the dissipation range is also used in some analyses. Such a model should be used when greater accuracy is needed for comparing theory with actual outdoor experimental data involving small-scale effects such as scintillation. The "modified atmospheric spectrum" is described by

$$\Phi_n(\kappa) = 0.033 C_n^2 \underbrace{\left[1 + 1.802\left(\frac{\kappa}{\kappa_l}\right) - 0.254\left(\frac{\kappa}{\kappa_l}\right)^{7/6}\right]}_{\text{Bump term}} \frac{\exp(-\kappa^2/\kappa_l^2)}{(\kappa^2 + \kappa_0^2)^{11/6}}, \quad 0 \le \kappa < \infty \tag{8}$$

where $\kappa_l = 3.3/l_0$ and $\kappa_0 = 2\pi/L_0$.[23] The bump in the spectrum was originally discovered in the temperature spectrum data of Champagne et al.[24] and in that of Williams and Paulson.[25] From these data, Hill later performed a hydrodynamic analysis and developed a numerical version of the bump spectrum for both temperature and refractive index.[26] Hill's numerical spectrum, however, did not include an outer scale parameter. This numerical spectrum model eventually led to the development of several analytical models.[23,27,28]

Another form of the modified atmospheric spectrum is sometimes used, which introduces the outer scale in an exponential function. This alternate form, which is used in the extended Rytov theory under moderate-to-strong turbulence conditions, is given by

$$\Phi_n(\kappa) = 0.033 C_n^2 \kappa^{-11/3} \underbrace{\left[1 + 1.802\left(\frac{\kappa}{\kappa_l}\right) - 0.254\left(\frac{\kappa}{\kappa_l}\right)^{7/6}\right]}_{\text{Bump term}} \exp\left(-\frac{\kappa^2}{\kappa_l^2}\right)\left[1 - \exp\left(-\frac{\kappa^2}{\kappa_0^2}\right)\right], \tag{9}$$

where $0 \le \kappa < \infty$, $\kappa_l = 3.3/l_0$ and $\kappa_0 = 8\pi/L_0$.

In Fig. 3, we plot scaled versions of the Kolmogorov, Tatarskii, and modified atmospheric spectrum models to illustrate their difference at high wave numbers. Scaling this way leads to a horizontal line for the Kolmogorov spectrum, whereas the inner scale behavior of the Tatarskii spectrum is shown by the dashed curve. For the modified atmospheric spectrum, the outer scale was chosen as infinite.

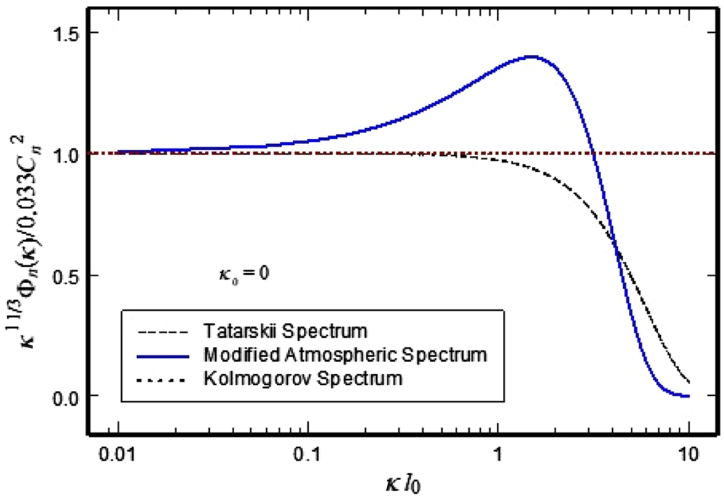


**Fig. 3** Spectrum models with $L_0 = \infty$, scaled by the Kolmogorov spectrum.[10]

In Secs. 5–7, we will separately discuss the models for scintillation index associated with plane waves, spherical waves and Gaussian-beam waves, respectively, after defining weak-to-strong intensity fluctuations in Sec. 4.

## 4 Weak-to-Strong Intensity Fluctuations

Although early research involved the log-amplitude parameter, the intensity was the parameter of interest as the research efforts turned toward applications. Thus, instead of relying on the log-amplitude parameter, the intensity parameter of interest became the "Rytov variance" $\sigma_R^2$. The parameter $\sigma_R^2$ is directly related to the log-amplitude variance by the expression $\sigma_R^2 = 4\sigma_\chi^2$.

Weak intensity fluctuations are characterized by requiring $\sigma_R^2 < 1$. Under this restriction, the "Rytov approximation" has been the most fruitful method of analysis, although the method of geometrical optics and the Born approximation were introduced first without much success.

When the Rytov variance satisfies $\sigma_R^2 > 1$, the intensity fluctuations are considered moderate to strong. In this case, we can perform the analysis with the "extended Rytov theory."[28,29] This theory is based on the following observations:

- The scintillation index increases with increasing values of the Rytov variance $\sigma_R^2$ until it reaches a maximum value greater than unity called the "focusing regime."
- With increasing values of $\sigma_R^2$, the focusing regime is weakened by multiple scattering and loss of spatial coherence, and then, the scintillation index begins to decrease, saturating at a level approaching unity from above. This is the "saturation regime."

This behavior of the scintillation index as described above is illustrated in Fig. 4 for the general case of a collimated beam wave. Similar behavior is also associated with plane and spherical waves.

So, the bottom line is as follows: The scintillation and power scintillation index equations in the Secs. 5–7 were developed using the extended Rytov theory and are valid for turbulence conditions covering weak to strong intensity fluctuations. Mathematically, the focusing and saturation effects are created by the inner and outer scales parts of the equations tempering the rising Rytov variance (which comes from increasing $C_n^2$, range or both) in the scintillation indices. The inner scale $l_0$ dominates the creation of the focusing regime, with a negligible contribution by the outer scale $L_0$. Effectively, $L_0 = \infty$ in these equations. However, as the Rytov variances move into the strong intensity fluctuation regime, the outer scale $L_0$ takes on the role of the dominant parameter. Specifically, the outer scale $L_0$ parts of the equation lower the inner scale $l_0$ contributions, resulting in lower saturation regime profiles. The above will be evident in the figures to come.

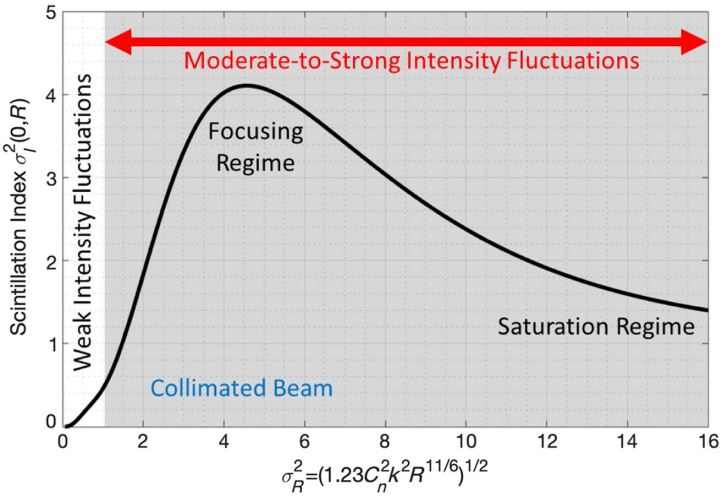


**Fig. 4** Typical behavior of scintillation as a function of the square root of the Rytov variance.

## 5 SATCOM Downlink (Plane Wave) Link Geometries

Many of the early laser propagation in turbulence studies were performed by Russian researchers using infinite plane wave models. As it turns out, the SATCOM downlink essentially created plane wave illumination at the ground station terminal.[10–12] Plane wave propagation in turbulence is the subject of this section.

### 5.1 Plane Wave: Weak Intensity Fluctuations

Based on the Rytov approximation,[10,11] the scintillation index for an infinite plane wave under weak intensity fluctuations can be written as

$$\sigma_{I,pl}^2(L) = 8\pi^2 k^2 L \int_0^1 \int_0^\infty \kappa \Phi_n(\kappa) \left[1 - \cos\left(\frac{L\kappa^2 \xi}{k}\right)\right] \mathrm{d}\kappa \, \mathrm{d}\xi \tag{10}$$

where $\xi = 1 - z/L$ is a normalized distance variable. It is assumed that the optical wave propagates on a slant path along the positive $z$-axis over the interval $0 =< z \leq L$. As noted in a previous section, the solution of this expression will depend on the power spectrum of index-of-refractive fluctuations.

Under the Kolmogorov spectrum, for example, the plane wave scintillation index becomes

$$\sigma_{I,pl}^2(L) = \sigma_R^2 = \begin{cases} 1.23 C_n^2 k^{7/6} L^{11/6}, & \text{(horizontal path)} \\ 2.25 k^{7/6} \int_{z_0}^L C_n^2(z)(z - z_0)^{5/6} \mathrm{d}z, & \text{(downlink path)} \end{cases}, \tag{11}$$

where both expressions represent the Rytov variance. If $h$ denotes altitude and $H$ is the satellite altitude, then it follows that $z = h/\cos\zeta$ and $L = H/\cos\zeta$, where $\zeta$ is the zenith angle.

Although many researchers rely on the Kolmogorov spectrum, which ignores inner and outer scale effects, we find that the inner scale plays an important role in the analysis of the scintillation index. Therefore, using the Tatarskii spectrum, the scintillation index of a plane wave takes the form

$$\sigma_{I,pl}^2(L) = 3.86\sigma_R^2 \left[\left(1 + \frac{1}{Q_m^2}\right)^{11/12} \sin\left(\frac{11}{6} \tan^{-1} Q_m\right) - \frac{11}{6} Q_m^{-5/6}\right], \tag{12}$$

where $Q_m = L\kappa_m^2/k$.[18] Because the Rytov variance requires the restriction $\sigma_R^2 < 1$ under weak intensity fluctuations, this restriction often limits the path length to a few hundred meters along a horizontal path, depending on $C_n^2$ and wavelength.

Based on the modified atmospheric spectrum model with $\kappa_0 = 0$, the scintillation index assumes the form[18]

$$\sigma_{PL}^2(L) = 3.86\sigma_R^2 \left\{\left(1 + \frac{1}{Q_l^2}\right)^{11/12} \left[\sin\left(\frac{11}{6} \tan^{-1} Q_l\right) + \frac{1.507}{(1 + Q_l^2)^{1/4}} \sin\left(\frac{4}{3} \tan^{-1} Q_l\right) - \frac{0.273}{(1 + Q_l^2)^{7/24}} \sin\left(\frac{5}{4} \tan^{-1} Q_l\right)\right] - \frac{3.50}{Q_l^{5/6}}\right\}. \tag{13}$$

Here, we define $Q_l = L\kappa_l^2/k$.

### 5.2 Plane Wave: Moderate-to-Strong Intensity Fluctuations

The atmosphere contains random inhomogeneities (turbulent "eddies") of many different scale sizes, ranging from exceptionally large scales such as the outer scale to small scales such as the inner scale. An optical wave propagating through such a medium will experience the effects of these random inhomogeneities in different ways, depending on the scale size. For example, large scales cause refractive effects that mostly distort the wavefront of the propagating wave. This effect can often be described by the method of geometrical optics. Small scales are mostly diffractive in nature and therefore distort the amplitude of the wave through beam spreading and intensity fluctuations. This behavior is now widely known as the "two-scale behavior" of the optical wave in turbulence.

Under weak intensity fluctuations, the Fresnel zone size $\sqrt{L/k}$ forms the division between large scales and small scales. After a wave propagates a sufficient distance $L$ into moderate-to-strong intensity fluctuations, only those turbulent eddies on the order of the transverse spatial

coherence radius $\rho_0$ or less are effective in producing further spreading and intensity fluctuations on the wave. Under strong intensity fluctuations, the spatial coherence radius also identifies a related large-scale eddy size near the transmitter (Tx) called the "scattering disk," $L/k\rho_0$. Here, $\rho_0$ is the spatial coherence radius of the optical wave. Basically, the scattering disk is defined by the refractive cell size at which the focusing angle is equal to the average scattering angle. Only eddy sizes equal to or larger than the scattering disk near the Tx can contribute to the field within the coherence area near the receiver (Rx). Thus, fewer and fewer scale sizes between the coherence radius and scattering disk contribute to the scintillation index. Also, the outer scale $L_0$ forms an upper bound on the largest eddy size forming a scattering disk and therefore becomes an important parameter in the moderate-to-strong fluctuation regime.

The theory developed here for moderate-to-strong intensity fluctuations is based on familiarity with the standard Rytov theory for weak fluctuations and with the deep turbulence theory for the saturation regime, so both can be used to help identify the transition scale sizes. Because the theory builds mostly off the standard Rytov theory, we call it the "extended Rytov theory."[10,29,30] In the absence of both inner and outer scale effects, the intensity is mainly affected by three cell sizes (eddies) described by

$$\begin{aligned} l_1 &\sim \rho_0 \quad \text{(spatial coherence radius)} \\ l_2 &\sim \sqrt{L/k} \quad \text{(Fresnel zone size)} \\ l_3 &\sim L/k\rho_0 \quad \text{(scattering disk)} \end{aligned} \tag{14}$$

As the optical wave propagates, there is a gradual transition from the Fresnel scale as the most critical cell size for scintillation to the spatial coherence radius and the scattering disk. That is, as the Fresnel zone scale approaches the size of the coherence radius at the onset of strong fluctuations ("focusing regime"), all three cell sizes are roughly equal ($l_1 \sim l_2 \sim l_3$). In approaching the focusing regime, the loss of spatial coherence affects eddies that are still strong enough to focus the beam. That is, large eddies near the Tx have the greatest focusing effect on the small eddies near the Rx. However, as the mid-size eddies become ineffective due to the loss of spatial coherence, the focusing effect is weakened, and the spatial coherence radius is smaller than the Fresnel zone, whereas the scattering disk is larger. We illustrate the relative cell size in Fig. 5 for a propagating plane wave.

The extended Rytov theory for the scintillation index makes use of known behavior in the weak intensity fluctuation regime and that in the far saturation regime. The saturation effect of scintillation under strong intensity fluctuations was first observed experimentally in 1965 by

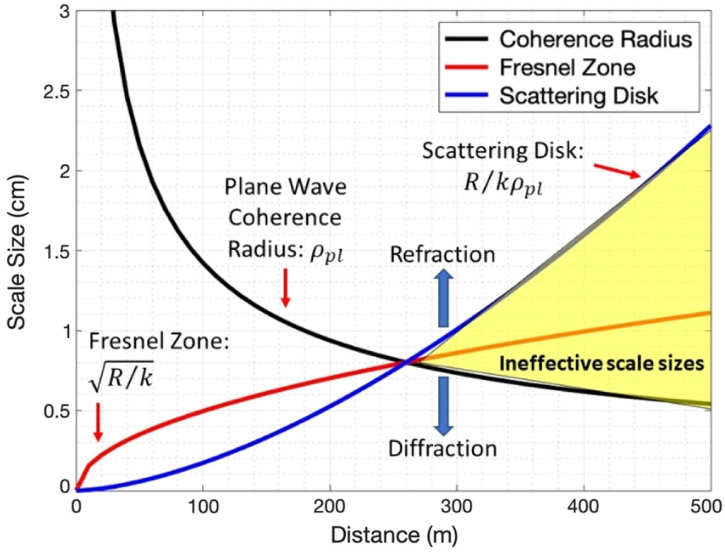


**Fig. 5** Relative turbulent scale sizes versus propagation distance for an infinite plane wave. The shaded area denotes unrealizable scale sizes under strong fluctuations.

Gracheva and Gurvich.[31] This work attracted much attention and stimulated several theoretical and experimental studies devoted to scintillation under strong intensity fluctuations.

Analytical models developed for the saturation regime are based on the "asymptotic theory" first introduced by Gochelashvili and Shishov[32] in 1974, followed by Fante[33] and Frehlich.[34]

Although it was first believed that the asymptotic theory would adequately predict the scintillation index throughout the moderate-to-strong fluctuation regime, this turned out to not be true. Including the inner scale in the models[33,34] did not help much. A failure of the asymptotic theory was eventually pointed out most clearly by Flatté and Gerber[35] who compared the asymptotic theory with simulation results for a spherical wave and found a poor match except far out in the saturation regime.

Based on the asymptotic theory, the scintillation index in the saturation regime for an infinite plane wave and Kolmogorov spectrum can be expressed as

$$\sigma_{I,pl}^2(L) = 3.86\sigma_R^2\left[\left(1+\frac{1}{Q_m^2}\right)^{11/12}\sin\left(\frac{11}{6}\tan^{-1}Q_m\right)-\frac{11}{6}Q_m^{-5/6}\right], \times\exp\left\{-\int_0^1 D_S\left[\frac{L\kappa}{k}w(\tau,\xi)\right]\mathrm{d}\tau\right\}\mathrm{d}\kappa\,\mathrm{d}\xi,\ \ \sigma_R^2\gg 1 \tag{15}$$

where $D_S(\rho)$ is the phase structure function and

$$w(\tau,\xi)=\begin{cases}\tau, & \tau<\xi\\ \xi, & \tau>\xi\end{cases}. \tag{16}$$

Upon evaluation of the integrals in Eq. (15), this leads to

$$\sigma_{I,pl}^2(L)\approx 1+\frac{0.86}{\sigma_R^{4/5}},\quad \sigma_R^2\gg 1. \tag{17}$$

When the inner scale is included, the asymptotic theory for a plane wave based on the modified atmospheric spectrum takes the form[15]

$$\sigma_{I,pl}^2(L)\approx 1+\frac{2.39}{(\sigma_R^2Q_l^{7/6})^{1/6}},\quad \sigma_R^2Q_l^{7/6}\gg 100, \tag{18}$$

where $Q_l = 10.89L/kl_0^2$. Similar expressions for the saturation regime have been reported for the spherical wave and Gaussian-beam wave.

To construct an atmospheric spectrum model for scintillation that characterizes the above behavior of the various cell sizes, a technique like that used in adaptive optics methods is introduced whereby the conventional Kolmogorov power-law spectrum is modified with a spatial filter. By also including the effects from inner scale and outer scale, this leads to the so-called "effective atmospheric spectrum,"

$$\Phi_{n,e}(\kappa)=\Phi_n(\kappa)G(\kappa,l_0,L_0,z), \tag{19}$$

where $\Phi_n(\kappa)$ is the conventional Kolmogorov spectrum and $G(\kappa,l_0,L_0,z)$ is an amplitude spatial filter. For horizontal paths in the positive $z$-direction for which turbulence parameters are essentially constant, such a spatial filter is represented by the sum of two filter functions, viz.,

$$\begin{aligned}G(\kappa,l_0,L_0,z) &= G_X(\kappa,l_0,L_0)+G_Y(\kappa,l_0,z)\\ &= \underbrace{f(\kappa l_0)g(\kappa L_0)\exp\left(-\frac{\kappa^2}{\kappa_X^2}\right)}_{G_X(\kappa,l_0,L_0)}+\underbrace{\frac{\kappa^{11/3}}{(\kappa^2+\kappa_Y^2)^{11/6}}\exp\left[\frac{\Lambda L\kappa^2(1-z/L)^2}{k}\right]}_{G_Y(\kappa,l_0,z)},\end{aligned} \tag{20}$$

where $f(\kappa l_0)$ describes inner scale modifications and $g(\kappa L_0)$ describes outer scale effects. Here, $\kappa_X$ is a large-scale spatial frequency cutoff, and $\kappa_Y$ is a small-scale spatial frequency cutoff. Thus, the filter function $G(\kappa,l_0,L_0,z)$ only permits low-pass spatial frequencies $\kappa<\kappa_X$ and high-pass spatial frequencies $\kappa>\kappa_Y$ at a given propagation distance $z$.

The inner scale filter function modification is defined by $f(\kappa l_0)=\exp(-\kappa^2/\kappa_l^2)$, and the outer scale modification is defined by $g(\kappa L_0)=1-\exp(-\kappa^2/\kappa_0^2)$, where $\kappa_0=8\pi/L_0$. The resulting scintillation index based on the modified atmospheric spectrum takes the form

$$\sigma_{I,pl}^2 = \exp\left[\sigma_{\ln X}^2(l_0) - \sigma_{\ln X}^2(l_0, L_0) + \frac{0.51\sigma_{PL}^2}{(1+0.69\sigma_{PL}^{12/5})^{5/6}}\right] - 1, \tag{21}$$

where

$$\sigma_{\ln X}^2(l_0) = 0.16\sigma_R^2\left(\frac{2.61Q_l}{2.61+Q_l+0.45\sigma_R^2Q_l^{7/6}}\right)^{7/6}\left\{1+1.75\left(\frac{2.61}{2.61+Q_l+0.45\sigma_R^2Q_l^{7/6}}\right)^{1/2} - 0.25\left(\frac{2.61}{2.61+Q_l+0.45\sigma_R^2Q_l^{7/6}}\right)^{7/12}\right\}, \tag{22}$$

$$\sigma_{\ln X}^2(l_0, L_0) = 0.16\sigma_R^2\left[\frac{2.61\hat{Q}_0Q_l}{2.61(\hat{Q}_0+Q_l)+\hat{Q}_0Q_l(1+0.45\sigma_R^2Q_l^{1/6})}\right]^{7/6} \times\left\{1+1.75\left[\frac{2.61\hat{Q}_0}{2.61(\hat{Q}_0+Q_l)+\hat{Q}_0Q_l(1+0.45\sigma_R^2Q_l^{1/6})}\right]^{1/2} -0.25\left[\frac{2.61\hat{Q}_0}{2.61(\hat{Q}_0+Q_l)+\hat{Q}_0Q_l(1+0.45\sigma_R^2Q_l^{1/6})}\right]^{7/12}\right\}, \tag{23}$$

and $\sigma_{PL}^2$ is given in Eq. (13). In these equations, we have $\hat{Q}_0 = 64\pi^2L/kL_0^2$. We have used the notation $\hat{Q}_0$ to avoid confusion with the outer scale parameter $Q_0$ defined in other publications.

Figure 6 illustrates the scintillation index of an infinite plane wave for a horizontal path as a function of the square root of the Rytov variance for several values of inner scale with infinite outer scale. This plot shows the importance of the inner scale along a horizontal path. The larger the inner scale, the lower the scintillation index for $\sigma_r > 1$.

If we ignore the inner and outer scale effects, we find that the moderate-to-strong scintillation index for a plane wave reduces to

$$\sigma_{I,pl}^2 = \exp\left\{\frac{0.49\sigma_R^2}{(1+1.11\sigma_R^{12/5})^{7/6}} + \frac{0.51\sigma_R^2}{(1+0.69\sigma_R^{12/5})^{5/6}}\right\} - 1, \quad 0 < \sigma_R^2 < \infty. \tag{24}$$

Because inner and outer scale models as a function of altitude are virtually nonexistent, this last expression is commonly used in downlink optical paths from a satellite or star. It is not very accurate for horizontal path propagation because the inner and outer scales play such dominant roles near the ground.

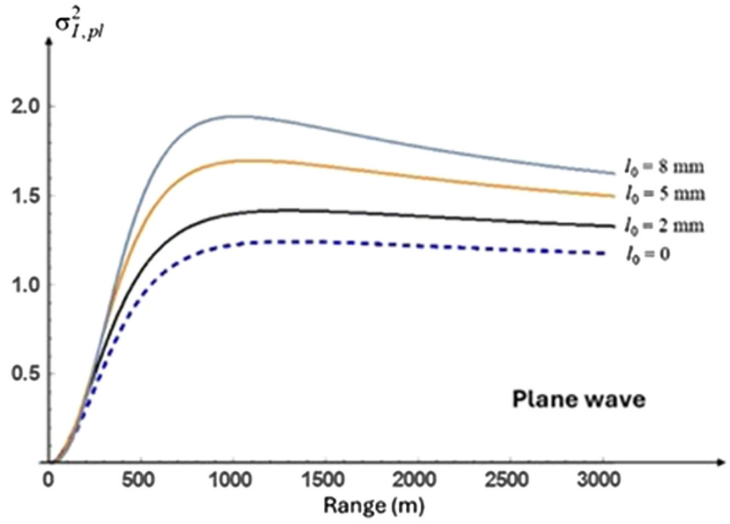


**Fig. 6** Plane wave scintillation index as a function of the square root of the Rytov variance for selected inner scale values between 0 and 8 mm, and $\lambda = 1063$ nm, $C_n^2 = 2\times10^{-13}$ m$^{-2/3}$, and $L_0 = \infty$, assuming a horizontal path.

### 5.3 Plane Wave: Aperture Averaging Effects

Early studies of aperture averaging concentrated on a ratio of scintillation values called the aperture-averaging factor. The aperture-averaging factor $A$ is defined by the normalized variance of power fluctuations of the incident optical field on a collecting lens. It is also defined by the ratio of the power scintillation index obtained by a finite-size collecting lens to the scintillation index obtained by a point aperture. For a circular aperture of diameter $D_{\mathrm{Rx}}$, this latter ratio, known as the aperture averaging factor, can be expressed by the integral

$$A = \frac{\sigma_{I,pl}^2(D_{Rx})}{\sigma_{I,pl}^2(0)} = \frac{16}{\pi}\int_0^1 b_I(xD_{\mathrm{Rx}})\left(\cos^{-1}x - x\sqrt{1-x^2}\right)x\mathrm{d}x, \tag{25}$$

where $b_I(xD_{Rx})$ is the normalized spatial covariance of the intensity fluctuations.[36] However, exact analytical solutions of Eq. (25) have not been found, so the first researchers always resorted to numerical evaluations or some approximations.[21,37] It was later shown that an alternate form for $\sigma_{I,\mathrm{pl}}^2(D_{\mathrm{Rx}})$ could be developed through the use of the "ABCD" ray matrix approach and the extended Rytov theory.[21]

FSOC systems that use a large collecting lens to focus the light onto a photo-detector do so in part to reduce the effects of scintillation. However, if the Rx aperture diameter $D_{\mathrm{Rx}}$ is smaller than the correlation width of the intensity fluctuations, then the Rx aperture behaves essentially like a point aperture. The correlation width under weak intensity fluctuations is on the order of the first Fresnel zone, $\sqrt{L/k}$, defined by the first zero value of the intensity covariance function.

Our approach here will follow that in Section 4.2 where the extended Rytov theory was introduced for the scintillation index. Consequently, the reduced scintillation index ("power scintillation index or flux variance") takes the form

$$\sigma_{I,pl}^2(D_{Rx}) = \exp[\sigma_{\ln X}^2(D_{Rx}, l_0) - \sigma_{\ln X}^2(D_{Rx}, l_0, L_0) + \sigma_{\ln Y}^2(D_{Rx})] - 1, \tag{26}$$

where

$$\sigma_{\ln X}^2(D_{Rx}, l_0) = 0.16\sigma_R^2\left(\frac{\eta_{Xd}Q_l}{\eta_{Xd}+Q_l}\right)^{7/6}\left[1 + 1.75\left(\frac{\eta_{Xd}Q_l}{\eta_{Xd}+Q_l}\right)^{1/2} - 0.25\left(\frac{\eta_{Xd}Q_l}{\eta_{Xd}+Q_l}\right)^{7/12}\right], \tag{27}$$

$$\sigma_{\ln X}^2(D_{Rx}, l_0, L_0) = 0.16\sigma_R^2\left(\frac{\eta_{Xd0}Q_l}{\eta_{Xd0}+Q_l}\right)^{7/6}\left[1 + 1.75\left(\frac{\eta_{Xd0}Q_l}{\eta_{Xd0}+Q_l}\right)^{1/2} - 0.25\left(\frac{\eta_{Xd0}Q_l}{\eta_{Xd0}+Q_l}\right)^{7/12}\right], \tag{28}$$

$$\sigma_{\ln Y}^2(D_{Rx}) = \frac{0.51\sigma_{PL}^2(1+0.69\sigma_{PL}^{12/5})^{-5/6}}{1+0.90d^2(\sigma_R^2/\sigma_{PL}^2)^{6/5}+0.62d^2\sigma_R^{12/5}}. \tag{29}$$

In the above equations, we have introduced the following parameters

$$\eta_X = \frac{2.61}{1+0.45\sigma_R^2 Q_l^{1/6}}, \quad \eta_{Xd} = \frac{\eta_X}{1+d^2\eta_X/4}, \quad \eta_{Xd0} = \frac{\eta_{Xd}\hat{Q}_0}{\eta_{Xd}+\hat{Q}_0},$$
$$d = \sqrt{\frac{kD_{Rx}^2}{4L}}, \quad Q_l = \frac{10.89L}{kl_0^2}, \quad \hat{Q}_0 = \frac{64\pi^2 L}{kL_0^2}. \tag{30}$$

If we ignore the inner and outer scale effects, the power scintillation index flux based on the Kolmogorov spectrum reduces to

$$\sigma_{I,pl}^2(D_{Rx}) = \exp\left[\frac{0.49\sigma_R^2}{(1+0.65d^2+1.11\sigma_R^{12/5})^{7/6}} + \frac{0.51\sigma_R^2(1+0.69\sigma_R^{12/5})^{-5/6}}{1+0.90d^2+0.62d^2\sigma_R^{12/5}}\right] - 1. \tag{31}$$

Figure 7 exhibits the plane wave aperture-averaging factor $A$ as a function of the circular aperture radius $D_{RX}/2$ scaled by the Fresnel zone size $\sqrt{L/k}$ under various values of the Rytov variance. Weak fluctuation theory corresponds to $\sigma_R^2 < 1$ in which the factor $A$ can be accurately approximated by

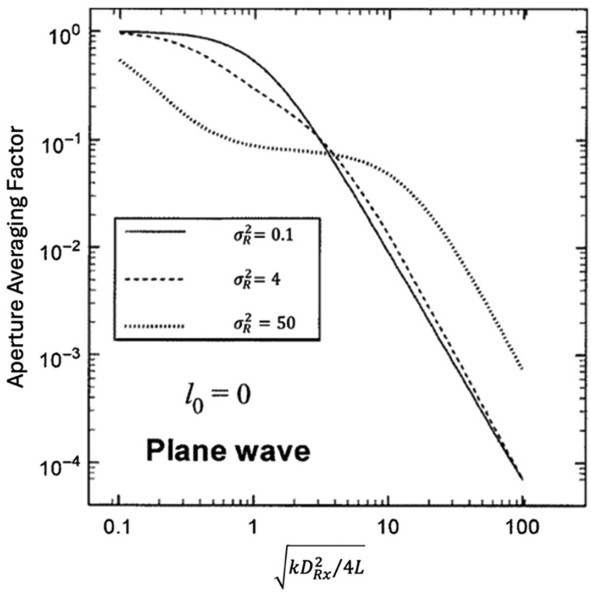


**Fig. 7** Aperture-averaging factor versus aperture radius scaled by the Fresnel zone size, $\sqrt{kD_{\mathrm{Rx}}/4L}$, associated with an unbounded plane wave under various fluctuation conditions.

$$A = \left[1 + 1.062\left(\frac{kD_{Rx}^2}{4L}\right)\right]^{-7/6}. \tag{32}$$

In weak conditions, the correlation scale of the irradiance fluctuations is defined by the size of the Fresnel zone; thus, significant aperture averaging takes place only when $D_{\mathrm{RX}} > 2\sqrt{L/k}$.

The case $\sigma_R^2 = 4$ leads to a scintillation index of $\sigma_I^2 = 1.17$, which corresponds to a moderate fluctuation level approaching the focusing regime. In this regime, the spatial coherence radius is less than or equal to the Fresnel zone size. The last case $\sigma_R^2 = 50$ corresponds to the saturation regime in which the scintillation index is once again $\sigma_I^2 = 1.17$. The two-scale behavior in the aperture-averaging factor in the saturation regime was previously pointed out by Churnside.[38] That is, the first averaging is determined by the spatial coherence scale $\rho_{PW}$, after which there is a leveling effect followed by a secondary roll-off related to the scattering disc $L/k\rho_{pl}$ that predicts less aperture averaging than that under weaker fluctuation conditions.

## 6 SATCOM Uplink (Spherical Wave) Link Geometries

The next stage in laser propagation in turbulence studies used spherical wave models. These studies pertained to SATCOM uplink illumination of the satellite terminal and certain FSOC cases involving horizontal links.[10–12]

### 6.1 Spherical Wave: Weak Intensity Fluctuations

If we can model the optical wave as a point source or spherical wave, the resulting scintillation index will closely follow that associated with the plane wave case. Making use of the Rytov theory, we define the scintillation index of a spherical wave by

$$\sigma_{I,sph}^2(L) = 8\pi^2 k^2 L \int_0^1 \int_0^\infty \kappa \Phi_n(\kappa)\left[1 - \cos\left(\frac{L\kappa^2\xi(1-\xi)}{k}\right)\right] \mathrm{d}\kappa\, \mathrm{d}\xi. \tag{33}$$

Based on the Rytov approximation and a Kolmogorov spectrum, the solution of Eq. (33) leads to

$$\sigma_{I,sph}^2(L) = \beta_0^2 = \begin{cases} 0.5C_n^2 k^{7/6} L^{11/6}, & \text{(horizontal path)} \\ 2.25k^{7/6} \int_{z_0}^{L} C_n^2(z)(z-z_0)^{5/6}[1-(z-z_0)/L]^{5/6} \mathrm{d}z, & \text{(uplink path)} \end{cases}. \tag{34}$$

In this last result, we have introduced the spherical wave Rytov variance $\beta_0^2 = 0.5C_n^2 k^{7/6} L^{11/6}$.

If we now evaluate Eq. (34) using the modified atmospheric spectrum, we get

$$\sigma_{SPH}^2 = 9.65\beta_0^2 \left\{ 0.40\left(1+\frac{9}{Q_l^2}\right)^{11/12} \left[ \sin\left(\frac{11}{6}\tan^{-1}\frac{Q_l}{3}\right) + \frac{2.610}{(9+Q_l^2)^{1/4}} \sin\left(\frac{4}{3}\tan^{-1}\frac{Q_l}{3}\right) - \frac{0.518}{(9+Q_l^2)^{7/24}} \sin\left(\frac{5}{4}\tan^{-1}\frac{Q_l}{3}\right) \right] - \frac{3.50}{Q_l^{5/6}} \right\}. \tag{35}$$

The effect of the inner scale on the scintillation index under weak intensity fluctuations is clearly illustrated in Fig. 8 for a spherical wave.[28] Several values of inner scale are featured here and compared with the scintillation index when $l_0 = 0$. As with plane waves, the outer scale is not a factor for the scintillation index of spherical waves under weak intensity fluctuations.

### 6.2 Spherical Wave: Moderate-to-Strong Intensity Fluctuations

Following a similar analysis to the above for plane waves, the resulting scintillation index based on the modified atmospheric spectrum takes the form

$$\sigma_{I,\mathrm{sph}}^2 = \exp\left[ \sigma_{\ln X}^2(l_0) - \sigma_{\ln X}^2(l_0, L_0) + \frac{0.51\sigma_{\mathrm{SPH}}^2}{(1+0.69\sigma_{\mathrm{SPH}}^{12/5})^{5/6}} \right] - 1, \tag{36}$$

where $\sigma_{\mathrm{SPH}}^2$ is given in Eq. (35). The first two terms in this last expression are

$$\sigma_{\ln X}^2(l_0) = 0.04\beta_0^2 \left( \frac{8.56Q_l}{8.56+Q_l+0.20\beta_0^2 Q_l^{7/6}} \right)^{7/6} \times \left\{ 1 + 1.75\left( \frac{8.56}{8.56+Q_l+0.20\beta_0^2 Q_l^{7/6}} \right)^{1/2} - 0.25\left( \frac{8.56}{8.56+Q_l+0.20\beta_0^2 Q_l^{7/6}} \right)^{7/12} \right\}, \tag{37}$$

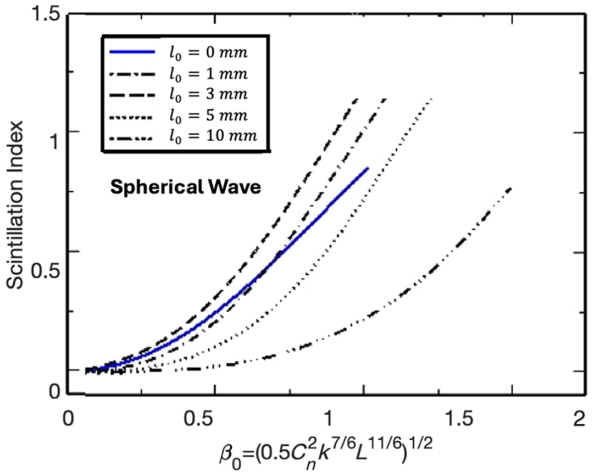


**Fig. 8** Scintillation index of a spherical wave based on the modified atmospheric spectrum as a function of the square root of the spherical wave Rytov variance and several values of inner scale.

$$\sigma^2_{\ln X}(l_0, L_0) = 0.04\beta_0^2 \left[\frac{8.56\hat{Q}_0 Q_l}{8.56(\hat{Q}_0 + Q_l) + \hat{Q}_0 Q_l (1 + 0.20\beta_0^2 Q_l^{1/6})}\right]^{7/6} \times \left\{1 + 1.75\left[\frac{8.56\hat{Q}_0}{8.56(\hat{Q}_0 + Q_l) + \hat{Q}_0 Q_l (1 + 0.20\beta_0^2 Q_l^{1/6})}\right]^{1/2} - 0.25\left[\frac{8.56\hat{Q}_0}{8.56(\hat{Q}_0 + Q_l) + \hat{Q}_0 Q_l (1 + 0.20\beta_0^2 Q_l^{1/6})}\right]^{7/12}\right\}. \quad (38)$$

Figure 9 illustrates the spherical wave scintillation index as a function of the spherical Rytov variance for $L_0 = \infty$ and several inner scale values. Compared with Fig. 6, the scintillation index falls off faster for spherical waves than for plane waves for all inner scale values but flattens out sooner for large inner scale values.

Figure 10 depicts the spherical wave scintillation index as a function of range up to 5 km illustrating the effect of the outer scale. The inner scale was fixed at 5 mm, and the outer scale was chosen as infinite and 1 m. In addition, the selected wavelength was 1063 nm and $C_n^2 = 5 \times 10^{-13}$ m$^{-2/3}$. This figure shows that the inner and outer scales cause the power

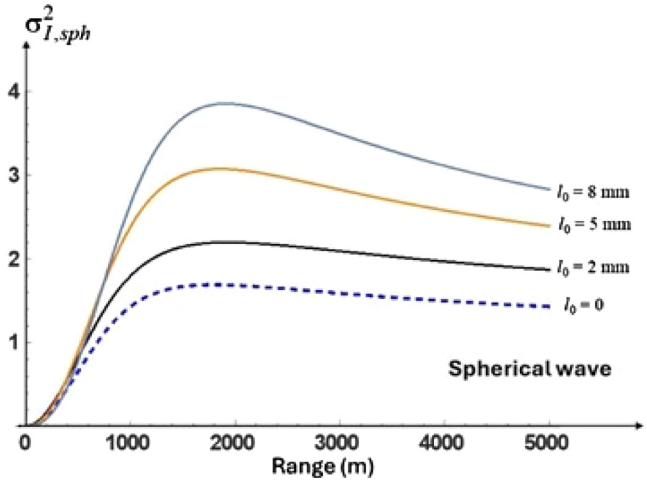


**Fig. 9** Scintillation index of a spherical wave as a function of the square root of the spherical wave Rytov variance and several values of inner scale, assuming $\lambda = 1063$ nm, $C_n^2 = 2 \times 10^{-13}$ m$^{-2/3}$, and $L_0 = \infty$.

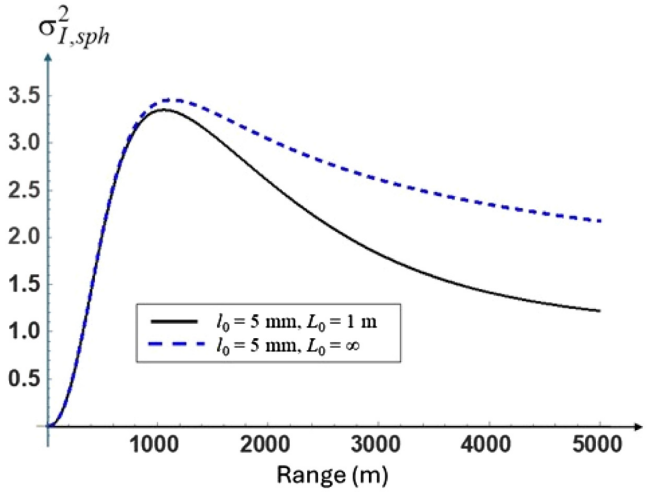


**Fig. 10** Scintillation index of a spherical wave as a function of range. The inner scale is 5 mm in both cases, and the outer scale is infinite (dashed line) or 1 m (solid line).

scintillation index to decrease for increasing range rather than leveling off like was seen in Fig. 1. Note that the outer scale effect does not show up prior to the focusing regime.

The effects of inner and outer scale on the scintillation index are further illustrated in Fig. 11 where the open circles correspond to measurements of a spherical wave made by Consortini et al.[39] over a horizontal path of 1200 m. A scintillometer was used to determine $C_n^2$, which ranged from $10^{-15}$ to $10^{-12}$ $m^{-2/3}$. The inner scale was measured with a separate instrument over a 150 m path directly in front of the Rx. The measured inner scale values ranged from 2.5 mm to around 12 mm. The optical wave was an argon-ion laser operating at 488 nm and the diverged beam was directed into the atmosphere at 1.2 m above ground. Stationary intervals of data with inner scale values ranging from 5 to 6 mm are replotted in Fig. 9 along with theoretical curves corresponding to inner scale values of 4 and 7 mm. The outer scale was estimated at 0.6 m, half the height of the laser above ground.

Once again, if we ignore inner scale and outer scale effects, we find that the moderate-to-strong scintillation index reduces to

$$\sigma_{I,sph}^2 = \exp\left\{\frac{0.49\beta_0^2}{(1+0.56\beta_0^{12/5})^{7/6}} + \frac{0.51\beta_0^2}{(1+0.69\beta_0^{12/5})^{5/6}}\right\} - 1, \quad 0 < \beta_0^2 < \infty. \tag{39}$$

The solid line in Fig. 12 shows the scintillation index as a function of range for $l_0 = 0$, $L_0 = \infty$, $\lambda = 1.55$ $\mu$m and $C_n^2(h_0) = 5 \times 10^{-15}$ $m^{-2/3}$.

### 6.3 Spherical Wave: Aperture Averaging Effects

Based on the extended Rytov theory for a plane wave, we again find that the general form of the power scintillation index for a spherical wave is defined by

$$\sigma_{I,sph}^2(D_{Rx}) = \exp[\sigma_{\ln X}^2(D_{Rx}, l_0) - \sigma_{\ln X}^2(D_{Rx}, l_0, L_0) + \sigma_{\ln Y}^2(D_{Rx})] - 1, \tag{40}$$

where the various terms are defined by

$$\sigma_{\ln X}^2(D_{Rx}, l_0) = 0.04\beta_0^2\left(\frac{\eta_{Xd}Q_l}{\eta_{Xd}+Q_l}\right)^{7/6} \times \left[1 + 1.75\left(\frac{\eta_{Xd}Q_l}{\eta_{Xd}+Q_l}\right)^{1/2} - 0.25\left(\frac{\eta_{Xd}Q_l}{\eta_{Xd}+Q_l}\right)^{7/12}\right], \tag{41}$$

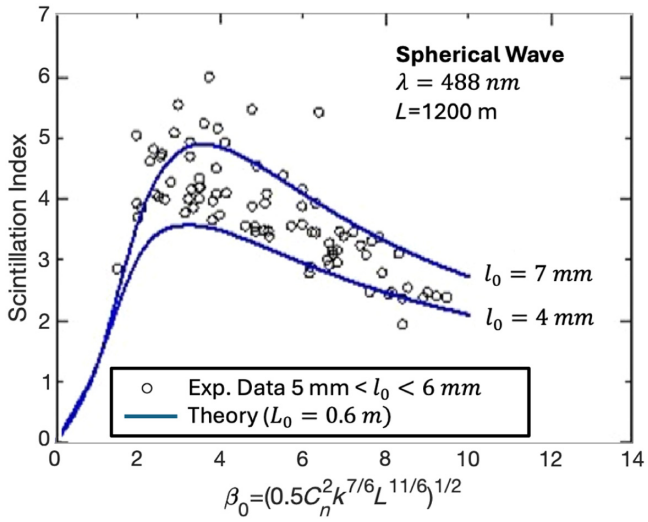


**Fig. 11** Estimates of measured scintillation index of a spherical wave (open circles) at a fixed propagation distance of 1200 m taken from[32] and replotted for measured inner scale values between 5 and 6 mm. The solid curves are theoretical estimates of the scintillation index corresponding to inner scale values of 4 and 7 mm along with an outer scale of 0.6 m.[16]

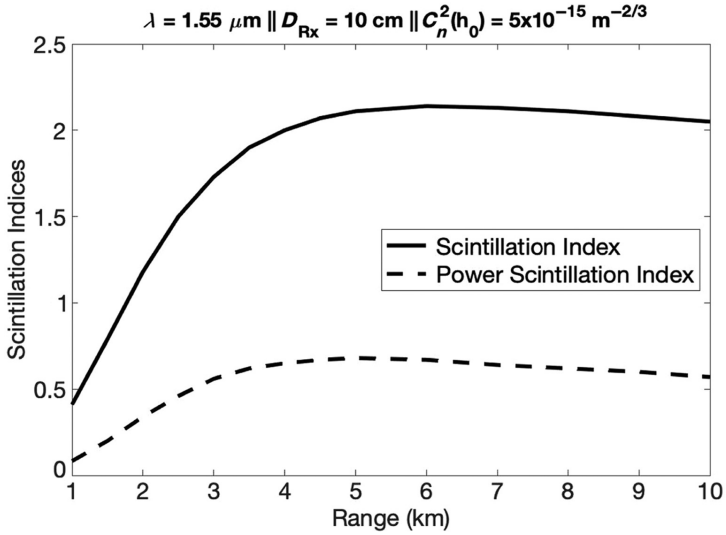


**Fig. 12** Scintillation index (solid line) and power scintillation indices (dashed line) as a function of the range for $\lambda = 1.55$ $\mu$m, $C_n^2(h_0) = 5 \times 10^{-15}$ m$^{-2/3}$, $l_0 = 0$, $L_0 = \infty$ and $D_{rx} = 10$ cm.

$$\sigma_{\ln X}^2(D_{Rx}, l_0, L_0) = 0.04\beta_0^2 \left(\frac{\eta_{Xd0} Q_l}{\eta_{Xd0} + Q_l}\right)^{7/6} \times \left[1 + 1.75\left(\frac{\eta_{Xd0} Q_l}{\eta_{Xd0} + Q_l}\right)^{1/2} - 0.25\left(\frac{\eta_{Xd0} Q_l}{\eta_{Xd0} + Q_l}\right)^{7/12}\right], \tag{42}$$

$$\sigma_{\ln Y}^2(D_{Rx}) = \frac{0.51\sigma_{SPH}^2(1 + 0.69\sigma_{SPH}^{12/5})^{-5/6}}{1 + 0.90d^2(\beta_0^2/\sigma_{SPH}^2)^{6/5} + 0.62d^2\beta_0^{12/5}}. \tag{43}$$

In this case, the above parameters are defined by

$$\eta_X = \frac{8.5}{1 + 0.20\beta_0^2 Q_l^{1/6}}, \quad \eta_{Xd} = \frac{\eta_X}{1 + 0.02d^2\eta_X}, \quad \eta_{Xd0} = \frac{\eta_{Xd}\hat{Q}_0}{\eta_{Xd} + \hat{Q}_0},$$
$$d = \sqrt{\frac{kD_{Rx}^2}{4L}}, \quad Q_l = \frac{10.89\,L}{kl_0^2}, \quad \hat{Q}_0 = \frac{64\pi^2 L}{kL_0^2}. \tag{44}$$

Finally, if we allow the inner scale to vanish and the outer scale to become infinite, the resulting power scintillation index of the spherical wave reduces to

$$\sigma_{I,\text{sph}}^2(D_{\text{Rx}}) = \exp\left[\frac{0.49\beta_0^2}{(1 + 0.18d^2 + 0.56\beta_0^{12/5})^{7/6}} + \frac{0.51\beta_0^2(1 + 0.69\beta_0^{12/5})^{-5/6}}{1 + 0.90d^2 + 0.62d^2\beta_0^{12/5}}\right] - 1. \tag{45}$$

The aperture-averaging factor for a spherical wave is defined by

$$A = \frac{\sigma_{I,\text{sph}}^2(D_{\text{Rx}})}{\sigma_{I,\text{sph}}^2(0)}. \tag{46}$$

Figure 12 also compares the scintillation index (solid line) and power scintillation indices (dashed line) as a function of the Rytov variance over horizontal link ranges from 1 to 10 km with $\lambda = 1.55$ $\mu$m, $C_n^2(h_0) = 5 \times 10^{-15}$ m$^{-2/3}$, $l_0 = 0$, $L_0 = \infty$, and $D_{\text{Rx}} = 10$ cm in the case of the power scintillation index. This plot follows the asymptotic trend shown in Fig. 1 and illustrates that aperture averaging can reduce the intensity-based intensity scintillation to a more desirable level for large $\sigma_R^2$.

Figure 13 illustrates the spherical wave aperture-averaging factor as a function of the circular aperture radius $D_{\text{Rx}}/2$ scaled by the Fresnel zone size $\sqrt{L/k}$ under various values of the spherical wave Rytov variance. The behavior shown in Fig. 13 is much the same as that in Fig. 7, except that the curves in Fig. 13 lie slightly above those in Fig. 7.

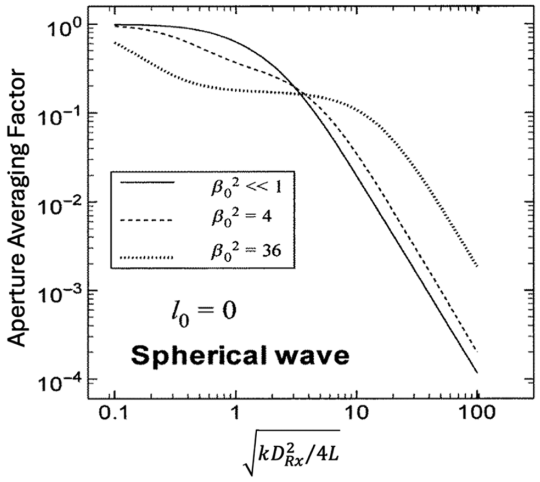


**Fig. 13** Aperture averaging factor versus aperture radius scaled by the Fresnel zone size, $\sqrt{kD_{Rx}/4L}$, associated with a spherical wave under various fluctuation conditions.

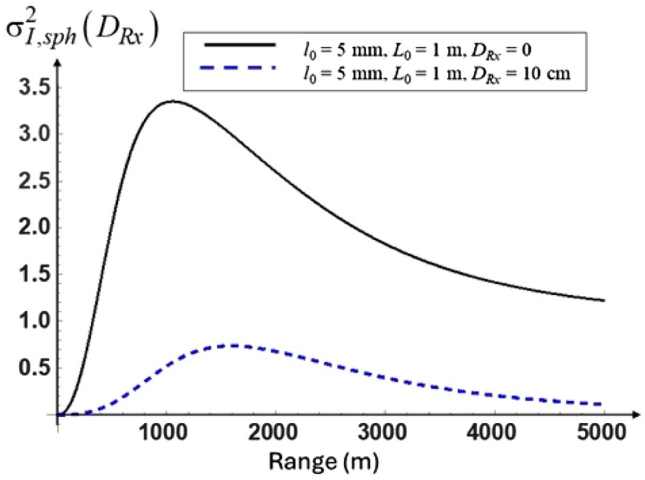


**Fig. 14** Power scintillation index in the pupil plane of an Rx (solid line) and that in the detector plane after passing through a 10-cm aperture. The inner scale is 5 mm, and the outer scale is 1 m in both curves.

Figure 14 shows the power scintillation index as a function of range for $D_{\mathrm{Rx}} = 0$ cm and $D_{\mathrm{Rx}} = 10$ cm, assuming $l_0 = 5$ mm and $L_0 = 1$ m. The wavelength and structure parameter are the same as that in Fig. 9. Comparing this figure with Fig. 11, the inclusion of the inner and outer scales causes the power scintillation index to decrease for increasing range (increasing $\sigma_R^2$) rather than leveling off. All these figures show that the inner and outer scales have a dramatic effect on the power scintillation index.

Figure 15 compares normalized power scintillation index theoretical estimates and computer simulation data as a function of $\sqrt{kD_{\mathrm{Rx}}/4L}$ for link ranges of 100 and 500 m. This figure shows good agreement between theory and computer simulation.

## 7 Horizontal (Gaussian-Beam) Link Geometries

Unlike in the plane and spherical wave cases described above, the Gaussian-beam scintillation index has two parts, not one part. One part is the radial component $\sigma_{I,r}^2(r, L)$, and the other is the longitudinal component $\sigma_{I,l}^2(0, L)$. The linear combination is written as

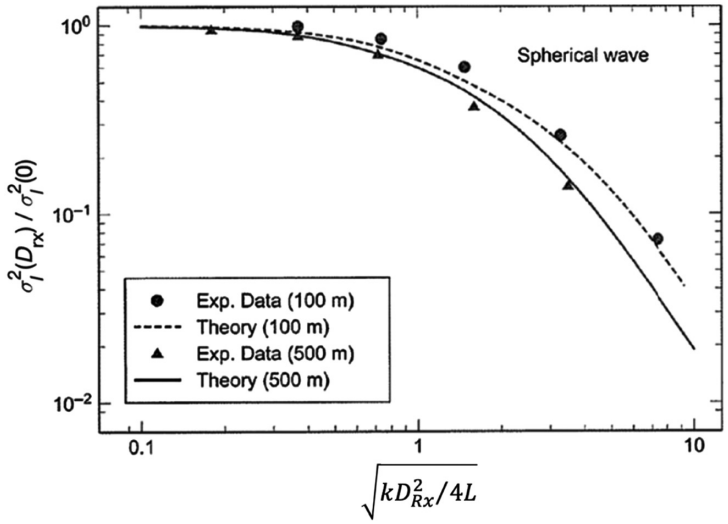


**Fig. 15** Comparison of the normalized power scintillation index theoretical estimates and computer simulation data as a function of $\sqrt{kD_{Rx}/4L}$ for link ranges of 100 and 500 m.

$$\sigma_I^2(r,L) = \sigma_{I,r}^2(r,L) + \sigma_{I,l}^2(0,L). \tag{47}$$

Although the Gaussian Beam normally is associated with horizontal link geometries, it also is applicable to slant range geometries, where the plane and spherical waves are opposite limiting cases. Specifically, the Rayleigh range is given by associated with a spherical wave, $\sqrt{kD_{Rx}/4L}$, under various fluctuation conditions.

$W_0$ is the $e^{-2}$-intensity beam radius.[10,11] When $z \ll z_R$, the propagating Gaussian beam is in the near field and is plane wave-like. When $z \gg z_R$, the propagating Gaussian beam is in the far field and is spherical wave-like. This section investigates the Gaussian beam scintillation indices.

### 7.1 Gaussian-Beam: Weak Intensity Fluctuations

Key to understanding Gaussian-beam propagation are two sets of nondimensional beam parameters—one set at the transmitter and a second set at the receiver at distance $L$. The beam radius is $W_0$, and the radius of curvature (focal length) is $f_{\mathrm{FL}}$. For the collimated transmitter, we have $f_{\mathrm{FL}} = \infty$, and the key parameter sets are given by

$$z_R = \pi W_0^2/\lambda = kW_0^2/2, \tag{48}$$

$$z = 0\colon\ \Theta_0 = 1 - \frac{L}{f_{FL}} = 1, \quad \Lambda_0 = \frac{2L}{kW_0^2} = \frac{8\lambda L}{\pi D_{tx}^2}, \tag{49}$$

whereas at the receiver, the corresponding beam parameters are

$$z = L\colon \begin{cases} \Theta = \frac{\Theta_0}{\Theta_0^2 + \Lambda_0^2}, \\ \overline{\Theta} = 1 - \Theta, \\ \Lambda = \frac{\Lambda_0}{\Theta_0^2 + \Lambda_0^2}. \end{cases} \tag{50}$$

In the above equations, $\Theta_0 = 1 - L/f_{\mathrm{FL}}$ describes the amplitude change due to refraction of focusing, $\Lambda_0$ describes the amplitude change due to aperture diffraction and [Ref. 11, pp. 18–19]

$$W = W_0\sqrt{\Theta_0^2 + \Lambda_0^2}. \tag{51}$$

Based on the modified atmospheric spectrum and weak intensity fluctuations, the longitudinal component of the Gaussian-beam scintillation index is given by

$$\sigma_G^2 \equiv \sigma_{I,l}^2(0,L) \approx 3.86\sigma_R^2\left\{0.40\frac{[(1+2\Theta)^2+(2\Lambda+3/Q_l)^2]^{11/12}}{[(1+2\Theta)^2+4\Lambda^2]^{1/2}}\right.$$
$$\times\left[\sin\left(\frac{11}{6}\varphi_2+\varphi_1\right)+\frac{2.610}{[(1+2\Theta)^2Q_l^2+(3+2\Lambda Q_l)^2]^{1/4}}\sin\left(\frac{4}{3}\varphi_2+\varphi_1\right)\right.$$
$$\left.-\frac{0.518}{[(1+2\Theta)^2Q_l^2+(3+2\Lambda Q_l)^2]^{7/24}}\sin\left(\frac{5}{4}\varphi_2+\varphi_1\right)\right]-\frac{13.401\Lambda}{Q_l^{11/6}[(1+2\Theta)^2+4\Lambda^2]}$$
$$\left.-\frac{11}{6}\left[\left(\frac{1+0.31\Lambda Q_l}{Q_l}\right)^{5/6}+\frac{1.096(1+0.27\Lambda Q_l)^{1/3}}{Q_l^{5/6}}-\frac{0.186(1+0.24\Lambda Q_l)^{1/4}}{Q_l^{5/6}}\right]\right\}, \quad (52)$$

for $\sigma_R^2 < 1$ where

$$\varphi_1 = \tan^{-1}\left[\frac{2\Lambda}{(1+2\Theta)}\right], \quad (53)$$

and

$$\varphi_2 = \tan^{-1}\left[\frac{(1+2\Theta)Q_l}{(3+2\Lambda Q_l)}\right]. \quad (54)$$

For horizontal FSOC links, the spherical-wave Fried parameters equal

$$r_{0Tx} = r_{0Rx} = [0.16k^2C_n^2(h_{tx})R]^{-3/5}. \quad (55)$$

### 7.2 Gaussian-Beam: Moderate to Strong Intensity Fluctuations

Using the extended Rytov theory to include the saturation regime ($0 =< \sigma_R^2 < \infty$) with both inner and outer scales, we find that components in Eq. (47) in this case are

$$\sigma_{I,r}^2(r,L) = 4.42\sigma_R^2\Lambda_{\mathrm{ST}}^{5/6}[1-1.15(L\Lambda_{\mathrm{ST}}/kL_0^2)^{1/6}]\frac{r^2}{W_{\mathrm{ST}}^2}, \quad (56)$$

and

$$\sigma_{I,l}^2(0,L) = \exp\left[\sigma_{\ln X}^2(l_0)-\sigma_{\ln X}^2(l_0,L_0)+\frac{0.51\sigma_G^2}{(1+0.69\sigma_G^{12/5})^{5/6}}\right]-1, \quad (57)$$

where

$$\Lambda_{ST} = wL/kW_{ST}^2, \quad (58)$$

$$W_{LT} = W(1+1.33\sigma_R^2\Lambda^{5/6})^{3/5}, \quad (59)$$

$$W_{ST} = \sqrt{W_{LT}^2-\langle r_c^2\rangle}, \quad (60)$$

and

$$\langle r_c^2\rangle = \frac{7.25(L-z_0)^2}{W_0^{1/3}}\int_{z_0}^{L}C_n^2(z)\left(1-\frac{z-z_0}{L-z_0}\right)^2\mathrm{d}z. \quad (61)$$

In Eq. (56), we have

$$\frac{\sigma_{\ln X}^2(l_0)}{0.49\sigma_R^2} = \left(\frac{1}{3}-\frac{1}{2}\overline{\Theta}+\frac{1}{5}\overline{\Theta}^2\right)\left(\frac{\eta_X Q_l}{\eta_X+Q_l}\right)^{7/6}\left[1+1.75\left(\frac{\eta_X}{\eta_X+Q_l}\right)^{1/2}-0.25\left(\frac{\eta_X}{\eta_X+Q_l}\right)^{7/12}\right], \quad (62)$$

$$\frac{\sigma_{\ln X}^2(l_0,L_0)}{0.49\sigma_R^2} = \left(\frac{1}{3}-\frac{1}{2}\overline{\Theta}+\frac{1}{5}\overline{\Theta}^2\right)\left(\frac{\eta_{X0} Q_l}{\eta_{X0}+Q_l}\right)^{7/6}$$
$$\times\left[1+1.75\left(\frac{\eta_{X0}}{\eta_{X0}+Q_l}\right)^{1/2}-0.25\left(\frac{\eta_{X0}}{\eta_{X0}+Q_l}\right)^{7/12}\right], \quad (63)$$

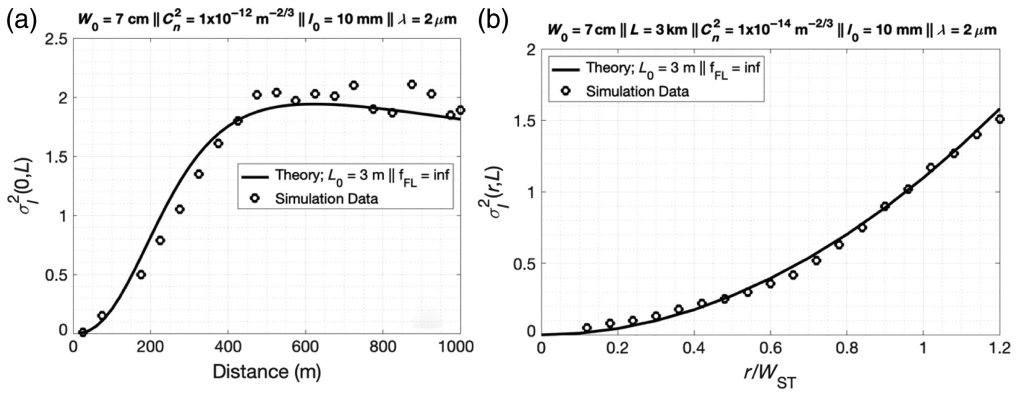


**Fig. 16** (a) On-axis and (b) off-axis Gaussian-beam wave scintillation indices as a function of propagation distance and normalized lateral radius, respectively.[10]

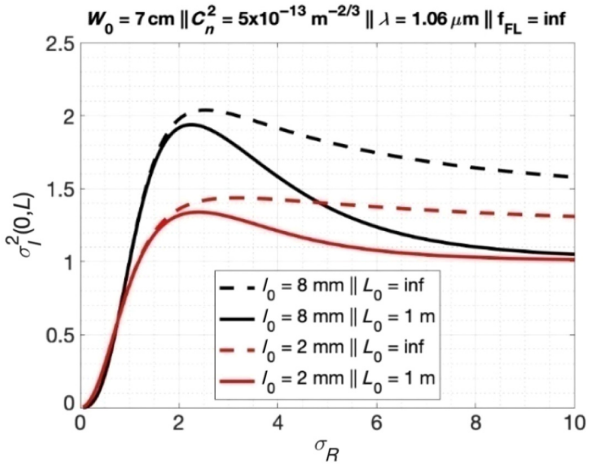


**Fig. 17** Graph of the scintillation index as a function of the square root of the Rytov variance for a couple of inner and outer scale values.

$$\eta_X = \left[0.38/(1-3.21\bar{\Theta}+5.92\bar{\Theta}^2)+0.47\sigma_R^2 Q_l^{1/6}\left(\left(\frac{1}{3}-\frac{1}{2}\bar{\Theta}+\frac{1}{5}\bar{\Theta}^2\right)/(1+2.20\bar{\Theta})\right)^{6/7}\right]^{-1}, \tag{64}$$

and

$$\eta_{X0} = \eta_X \hat{Q}_0/(\eta_X + \hat{Q}_0). \tag{65}$$

Figure 16 compares (a) on-axis and (b) off-axis Gaussian-beam wave scintillation indices as a function of propagation distance and normalized lateral radius, respectively, with computer simulation data. These figures show good agreement between theory and computer simulation.

Figure 17 illustrates the scintillation index as a function of the square root of the Rytov variance for a couple of inner and outer scale values. This figure shows that a smaller outer scale reduces the scintillation index. In addition, it shows that a smaller inner scale reduces the scintillation index, but the two outer scale curves begin to converge as $\sigma_R$ becomes large. NOTE: Outer scale effects occur only after peak scintillation values. The inner scale alters the scintillation index for all Rytov values.

### 7.3 Gaussian-Beam: Beam Wander

Beam wander associated with a propagating finite beam in the atmosphere has consequences on several characteristics of the beam irradiance in the plane of an Rx, including the short-term and long-term spot size, and the scintillation index. The total beam-wander variance along a

horizontal path is given by $\langle r_c^2 \rangle = 2.42 C_n^2 L^3 W$, which is related to centroid wander by $\langle \beta_c^2 \rangle = 0.56 \langle r_c^2 \rangle$. Beam wander occurs along horizontal paths or along uplink slant paths if the beam is not tracked.

Perhaps the most important consequence connected to beam wander is the increase in the scintillation index. It has been shown that beam-wander-induced scintillation can be modeled by adding the term $4.42\sigma_R^2 \Lambda_{ST}^{5/6} \sigma_{pe}^2 / W_{ST}^2$ to the scintillation index given by Eq. (47) using Eq. (57), i.e.,

$$\sigma_{I,l}^2(0,L) = 4.42\sigma_R^2 \Lambda_{ST}^{5/6} \frac{\sigma_{pe}^2}{W_{ST}^2} + \exp\left[\sigma_{\ln X}^2(l_0) - \sigma_{\ln X}^2(l_0, L_0) + \frac{0.51\sigma_G^2}{(1+0.69\sigma_G^{12/5})^{5/6}}\right] - 1, \quad (66)$$

where $\sigma_{pe}^2$ acts as a type of pointing error described by

$$\sigma_{pe}^2 = \langle r_c^2 \rangle \left[1 - \left(\frac{\pi^2 W_0^2/25 r_0^2}{1+\pi^2 W_0^2/25 r_0^2}\right)^{1/6}\right]. \quad (67)$$

The parameters $\Lambda_{ST}$ and $W_{ST}$ are defined by Eqs. (58) and (60), respectively. For the remainder of this paper, we will assume that the FSOC terminal has tip/tilt tracking capabilities.

### 7.4 Gaussian-Beam: Aperture Averaging Effect

In the presence of the inner and outer scales, the tip/tilt-tracked scintillation index in the detector plane equals

$$\sigma_{I,\text{Tip-Tilt}}^2(D_{Rx}) = \exp[\sigma_{\ln X}^2(D_{Rx}, l_0) - \sigma_{\ln X}^2(D_{Rx}, l_0, L_0) + \sigma_{\ln Y}^2(D_{Rx})] - 1. \quad (68)$$

In Eq. (68), we have

$$\frac{\sigma_{\ln X}^2(D_{Rx}, l_0)}{0.49\sigma_R^2} = \left(\frac{\Omega_{Rx}-\Lambda}{\Omega_{Rx}+\Lambda}\right)^2 \left(\frac{1}{3} - \frac{1}{2}\overline{\Theta} + \frac{1}{5}\overline{\Theta}^2\right) \left(\frac{\eta_{Xd} Q_l}{\eta_{Xd}+Q_l}\right)^{7/6} \times \left[1 + 1.75\left(\frac{\eta_{Xd}}{\eta_{Xd}+Q_l}\right)^{1/2} - 0.25\left(\frac{\eta_{Xd}}{\eta_{Xd}+Q_l}\right)^{7/12}\right], \quad (69)$$

$$\frac{\sigma_{\ln X}^2(D_{Rx}, l_0, L_0)}{0.49\sigma_R^2} = \left(\frac{\Omega_{Rx}-\Lambda}{\Omega_{Rx}+\Lambda}\right)^2 \left(\frac{1}{3} - \frac{1}{2}\overline{\Theta} + \frac{1}{5}\overline{\Theta}^2\right) \left(\frac{\eta_{Xd0} Q_l}{\eta_{Xd0}+Q_l}\right)^{7/6} \times \left[1 + 1.75\left(\frac{\eta_{Xd0}}{\eta_{Xd0}+Q_l}\right)^{1/2} - 0.25\left(\frac{\eta_{Xd0}}{\eta_{Xd0}+Q_l}\right)^{7/12}\right], \quad (70)$$

$$\sigma_{\ln Y}^2(D_{Rx}, l_0) = \frac{1.27\sigma_R^2 \eta_Y^{-5/6}}{1+0.40\eta_Y/(\Omega_{Rx}+\Lambda_1)}, \quad (71)$$

$$\eta_X = \left[0.38/(1-3.21\overline{\Theta}+5.92\overline{\Theta}^2) + 0.47\sigma_R^2 Q_l^{1/6}\left(\left(\frac{1}{3} - \frac{1}{2}\overline{\Theta} + \frac{1}{5}\bar{\Theta}^2\right)/(1+2.20\overline{\Theta})\right)^{6/7}\right]^{-1}, \quad (72)$$

and

$$\eta_Y = 3(\sigma_R/\sigma_G)^{12/5}(1+0.69\,\sigma_G^{12/5}) \quad (73)$$

where $\eta_{Xd0} = \eta_{Xd}\hat{Q}_0/(\eta_{Xd}+\hat{Q}_0)$, $\eta_{Xd} = \eta_X/[1+0.40\eta_X(2-\overline{\Theta}_1)/(\Omega_{Rx}+\Lambda_1)]$ and

$$\sigma_{pe}^2 = \frac{2.42 C_n^2(h_{tx}) R^3}{W_0^{1/3}} \left[1 - \left(\frac{\pi^2 W_0^2/25 r_0^2}{1+\pi^2 W_0^2/25 r_0^2}\right)^{1/6}\right]. \quad (74)$$

The example in the Sec. 8 will utilize these equations.

## 8 Bit Error Rate Analysis Example

The electrical SNR for a horizontal FSOC link in turbulence is written as

$$\mathrm{SNR}_e(I') \approx \frac{P_{\mathrm{rec}}^2(I')}{(\mathrm{NEP}_{\mathrm{det}})^2 + \sigma_I^2(D_{\mathrm{Tx}})\langle I(0,R)\rangle^2} = \frac{Q_I^2(I')^2}{(\mathrm{NEP}_{\mathrm{det}})^2 + \sigma_I^2(D_{\mathrm{Tx}})Q_I^2\langle I(0,R)\rangle^2}, \tag{75}$$

$$= \frac{\mathrm{SNR}_e^{\mathrm{sys}}(I')^2}{1 + \sigma_I^2(D_{\mathrm{Tx}})\mathrm{SNR}_e^{\mathrm{sys}}}. \tag{76}$$

where

$$Q_I = \gamma_{\mathrm{rx}}\gamma_{\mathrm{fiber}}A_{\mathrm{rx}}\mathrm{SR}_{\mathrm{DP}}. \tag{77}$$

and

$$\mathrm{SNR}_e^{\mathrm{sys}} \approx \frac{P_{\mathrm{avg}}^2}{(\mathrm{NEP}_{\mathrm{sys}})^2} = \frac{(\gamma_{\mathrm{rx}}\langle I(0,R)\rangle A_{\mathrm{rx}}\mathrm{SR}_{\mathrm{DP}})^2}{(\mathrm{NEP}_{\mathrm{sys}})^2} = Q_I^2\langle I(0,R)\rangle^2, \tag{78}$$

as the signal and background shot noise typically are much less than system noise. The extra term in the SNR denominator comes from the fact that the noise variance from the turbulence-degraded intensity is written as

$$\sigma_{\mathrm{Noise\text{-}turb}}^2 = \langle I_{\mathrm{turb}}^2(0,R)\rangle - \langle I(0,R)\rangle^2 = \langle I(0,R)\rangle\sigma_I^2(0,R) = \langle I(0,R)\rangle\sigma_I^2(D_{tx}), \tag{79}$$

where $\sigma_I^2(0,R)$ is the scintillation index. In these equations, we have replaced $\sigma_I^2(0,R)$ with $\sigma_I^2(D_{rx})$, the power scintillation index that accounts for aperture averaging. Let us now investigate its calculation.

The BER for a differential phase shift key (DPSK) communications system in the absence of turbulence is given by

$$\mathrm{BER} = 0.5\,\mathrm{erfc}\left(\sqrt{\mathrm{SNR}_e/2}\right), \tag{80}$$

where $\mathrm{erfc}(x)$ is the complementary error function.

Assuming tip/tilt correction, the unconditional BER in the presence of turbulence-induced beam wander should be averaged with respect to the DPSK BER to yield the average BER. It is written as

$$\overline{\mathrm{BER}} = 0.5\int_0^\infty p_{\ln I}(I')\mathrm{erfc}\left(\frac{1}{\sqrt{2}}\sqrt{\frac{\mathrm{SNR}_e^{\mathrm{sys}}(I')^2}{1+\sigma_I^2(D_{\mathrm{Tx}})\mathrm{SNR}_e^{\mathrm{sys}}}}\right)\mathrm{d}I' \tag{81}$$

where $\sigma_I^2(D_{tx})$ is the power scintillation index and $p_{\ln I}(I')$ is the log-normal (LN) PDF, which is given as

$$p_{\ln I}(I') = \frac{1}{I'\sqrt{2\pi\sigma_{\ln I}^2(D_{\mathrm{rx}})}}\exp\left\{-\frac{[\ln(I') + 0.5\sigma_{\ln I}^2(D_{\mathrm{rx}})]^2}{2\sigma_{\ln I}^2(D_{\mathrm{rx}})}\right\} \tag{82}$$

with $\sigma_{\ln I}^2(D_{\mathrm{Rx}}) = \ln[1+\sigma_I^2(D_{\mathrm{Rx}})]$, which is valid in the weak-to-moderate intensity fluctuations regimes when the receiver aperture is large.[40,41]

Let us assume a horizontal 1.5 km, DPSK FSOC link where the transmitter and receiver terminals are located at an elevated height above the ground. If the turbulence has a refractive index structure parameter $C_n^2(h_0)$ at the transmitter/receiver altitude $h_0$ equals $10^{-14}$ $\mathrm{m}^{-2/3}$ with an 3 mm inner scale and an 5 m outer scale, the resulting average BER as a function of the system-noise-limited SNR for uncoded and selected Reed-Solomon coded data streams[42] is shown in Fig. 18(a). Also exhibited in the figure is the required free-space electrical SNR of 16.94 dB for a required BER of $10^{-12}$. This figure clearly shows that the uncoded data stream does not meet the required BER for all system-noise-limited SNRs. However, a Reed–Solomon RS (255,247) code gives the required or better BER for SNRs > 15 dB.

If $C_n^2(h_0) = 5\times10^{-14}$ $\mathrm{m}^{-2/3}$, the resulting BER plot is depicted in Fig. 18(b). This figure clearly shows that the uncoded data stream again does not meet the required BER for all system-noise-limited SNRs and a Reed–Solomon RS (255,231) code gives the required or better BER for SNRs greater than 15 dB.

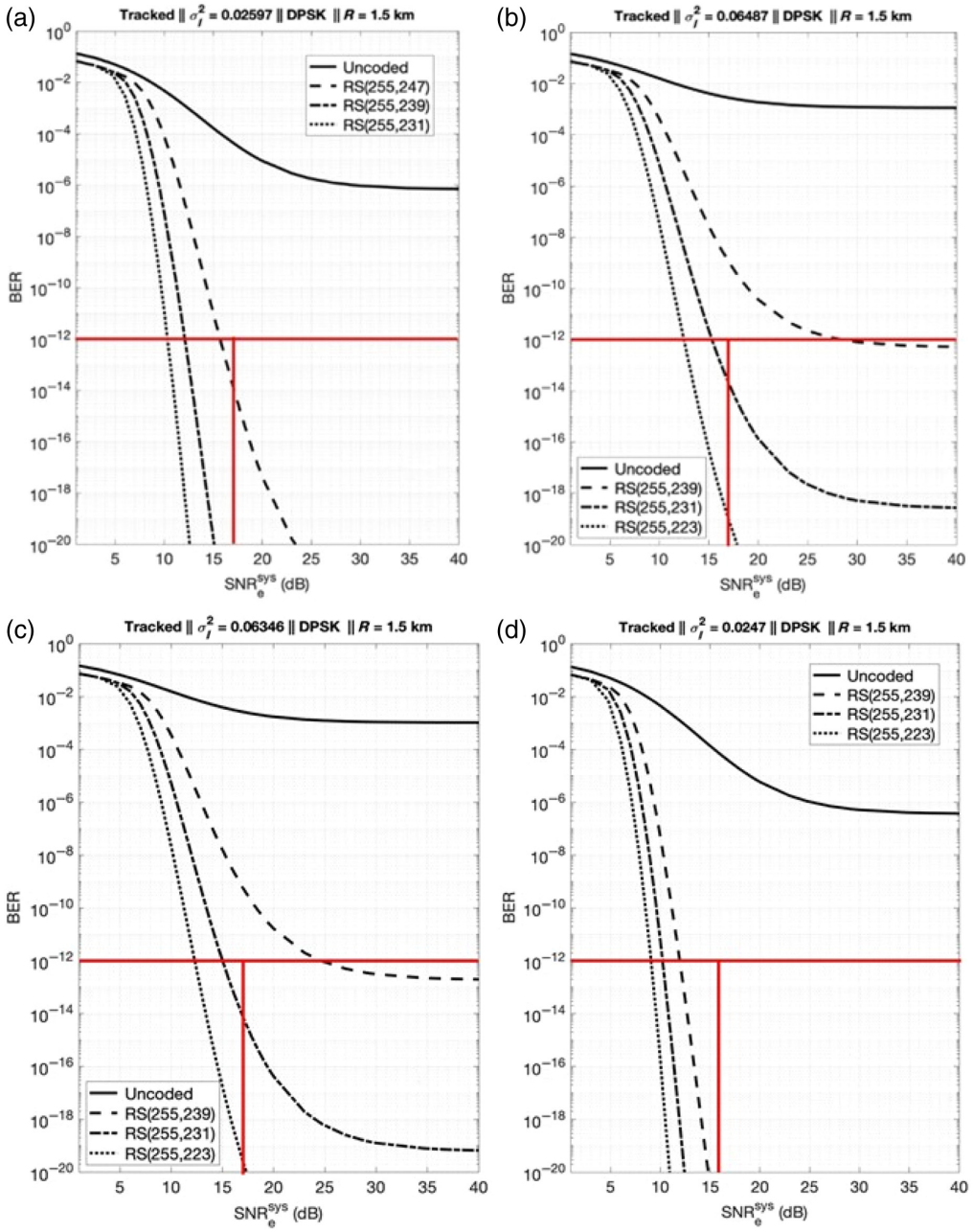


**Fig. 18** BER as a function of the system-noise-limited SNR for uncoded and selected Reed-Solomon Coded data streams for (a) $C_n^2(h_0) = 10^{-14}$ m$^{-2/3}$, (b) $C_n^2(h_0) = 5 \times 10^{-14}$ m$^{-2/3}$, (c) $C_n^2(h_0) = 10^{-13}$ m$^{-2/3}$, and (d) $C_n^2(h_0) = 5 \times 10^{-13}$ m$^{-2/3}$.

If $C_n^2(h_0) = 1 \times 10^{-13}$ m$^{-2/3}$, one has a refractive index structure parameter level commensurate with 5xHufnagel-Valley turbulence (85% CDF level), and the resulting BER plot is depicted in Fig. 18(c). This figure clearly shows that its power scintillation index is just slightly smaller than the $C_n^2(h_0) = 5 \times 10^{-14}$ m$^{-2/3}$ power scintillation index and the Reed–Solomon RS (255,231) code still gives the required or better BER for SNRs greater than 15 dB.

If $C_n^2(h_0) = 5 \times 10^{-13}$ m$^{-2/3}$, the resulting BER plot is depicted in Fig. 18(d). This figure clearly shows that its power scintillation index is smaller than the $C_n^2(h_0) = 10^{-13}$ m$^{-2/3}$ power scintillation index and the Reed–Solomon RS (255,239) and RS (255,231) codes still give the required or better BER for SNRs greater than 15 dB. As it turns out at this point, increasing the refractive index structure parameter gives an even smaller power scintillation index. This is because the scintillation and the power scintillation indices both decrease as the Rytov variance

moves out of the focusing regime. This was seen in earlier figures. The Rytov variances $\sigma_R^2$ equal 0.419, 2.09, 4.182, and 20.9 for refractive index structure parameters $10^{-14}$ $m^{-2/3}$; $5 \times 10^{-14}$ $m^{-2/3}$; $10^{-13}$ $m^{-2/3}$; and $5 \times 10^{-13}$ $m^{-2/3}$, respectively. In our case, the power scintillation peaks around Rytov variances between 2 and 4 and decreases for larger variances. Referring to the previous figures, using an RS (255,231) code will allow the DPSK system to meet or exceed the required BER for all expected turbulence conditions. The penalty is that the information rate is now 90.6% of the system data rate.

## 9 Summary

This paper provides a tutorial describing the various scintillation index and power scintillation index that follow the type of performance depicted in Fig. 1. Specifically, this paper developed the scintillation indices for SATCOM downlink, SATCOM uplink, and atmospheric slant path and horizontal communications link geometries, which also included tracking, untracked, and aperture averaging receiver effects. These scintillation index equations are valid for turbulence conditions covering weak to strong intensity fluctuations. Example figures showed that the focusing and saturation effects were created by the inner and outer scales parts of the equations tempering the rising Rytov variance in the scintillation indices. The inner scale dominated the creation of the scintillation index profiles in the focusing regime, whereas the outer scale dominated the creation of the scintillation index profiles in the saturation regime. An example analysis was performed using this information. The conclusion was that no matter whether the detection system is incoherent or coherent and/or which signaling format is used, the scintillation indices will have peak values for some particular $C_n^2(h_0)$ and $L$ values as those entities increase. This means that the deep turbulence system performance may be more easily achieved because of the peaking of those entities in that regime.

### Disclosures

The authors declare that there are no conflicts of interest related to this article.

### Code and Data Availability

Experimental data presented in this paper may be obtained from the cited authors upon reasonable request.

### References


1. C. Chen et al., "Demonstration of a bidirectional coherent air-to-ground optical link," *Proc. SPIE* **10524**, 105240G (2018).
2. H. Kaushal and G. Kaddoum, "Optical communication in space: challenges and mitigation techniques," *IEEE Commun. Surv. Tut.* **19**(1), 57–96 (2017).
3. L. B. Stotts, *Free Space Optical Systems Engineering*, John Wiley and Sons (2017).
4. A. Mansour, R. Mesleh, and M. Abaza, "New challenges in wireless and free space optical communications," *Opt. Lasers Eng.* **89**, 95–108 (2017).
5. S. Seel et al., "Space to Ground bidirectional optical communication link at 5.6 Gbps and EDRS connectivity outlook," in *Aerosp. Conf.*, Big Sky, MT, USA, pp. 1–7 (2011).
6. R. Lange et al., "142 km, 5.625 Gbps free—space optical link based on homodyne BPSK modulation," *Proc. SPIE* **6105**, 61050A (2006).
7. Z. C. Bagley et al., "Hybrid optical radio frequency airborne communications," *Opt. Eng.* **51**, 055006 (2012).
8. J. C. Juarez et al., "Analysis of link performance for the FOENEX laser communications system (Proceedings Paper)," *Proc. SPIE* **8380**, 838007 (2012).
9. L. B. Stotts, M. Toyoshima, and L. C. Andrews, "Effect of satellite slew rate in bit error rate model under atmospheric turbulence," *Proc. SPIE* **13355**, 13355-53 (2025).
10. L. C. Andrews and R. L. Phillips, *Laser Beam Propagation through Random Media*, 2nd ed., SPIE Press, Bellingham, Washington (2005).
11. L. C. Andrews. *Field Guide to Atmospheric Optics*, 2nd ed., SPIE Press, Bellingham, Washington (2019).
12. L. C. Andrews and M. K. Beason, *Laser Beam Propagation through Random Media: New and Advanced Topics*, SPIE Press, Bellingham, Washington (2023).

13. R. R. Beland, "Propagation through atmospheric optical turbulence," in *The Infrared and Electro-Optical Systems Handbook*, Vol. **2**, The Environmental Research Institute of Michigan and SPIE Press, Bellingham, Washington (1996).
14. M. E. Gracheva, "Investigation of the statistical properties of strong fluctuations in the intensity of light propagated through the atmosphere near the earth," *Radiophys. Quantum Electron.* **10**, 424–433 (1967).
15. R. A. Schmeltzer, "Means, variances and covariances for laser beam propagation through a random medium," *Q. Appl. Math.* **24**, 339–354 (1967).
16. D. L. Fried and J. B. Seidman, "Laser beam scintillations in the atmosphere," *J. Opt. Soc. Amer.* **57**, 181–185 (1967).
17. A. Ishimaru, "Fluctuations of a beam wave propagating through a locally homogeneous medium," *Radio Sci.* **4**, 295–305 (1969).
18. W. B. Miller, J. C. Ricklin, and L. C. Andrews, "Effects of the refractive index spectral model on the intensity variance of a Gaussian beam," *J. Opt. Soc. Amer. A* **11**, 2719–2726 (1994).
19. L. C. Andrews, R. L. Phillips, and C. Y. Hopen, *Laser Beam Scintillation with Applications*, SPIE Press, Bellingham, Washington (2001).
20. A. H. Mikesell, A. A. Hoag, and J. S. Hall, "The scintillation of starlight," *J. Opt. Soc. Amer.* **41**, 689–695 (1951).
21. L. C. Andrews, R. L. Phillips, and C. Y. Hopen, "Aperture averaging of optical scintillations: power fluctuations and the temporal spectrum," *Waves Random Media* **10**, 53–70 (2000).
22. L. F. Richardson, *Weather Prediction by Numerical Process*, Cambridge University Press (1922).
23. L. C. Andrews, "An analytical model for the refractive index power spectrum and its application to optical scintillations in the atmosphere," *J. Mod. Opt.* **39**, 1849–1853 (1992).
24. F. H. Champagne et al., "Flux measurements, flux-estimation techniques, and fine-scale turbulence measurements in the unstable surface layer over land," *J. Atmos. Sci.* **34**, 515–530 (1977).
25. R. M. Williams and C. A. Paulson, "Microscale temperature and velocity spectra in the atmospheric boundary layer boundary layer," *J. Fluid Mech.* **83**, 547–567 (1977).
26. R. J. Hill, "Models of the scalar spectrum for turbulent advection," *J. Fluid Mech.* **88**, 541–562 (1978).
27. J. H. Churnside, "A spectrum of refractive-index turbulence in the turbulent atmosphere," *J. Mod. Opt.* **37**, 13–16 (1990).
28. R. Frehlich, "Laser scintillation measurements of the temperature spectrum in the atmospheric surface layer," *J. Atmos. Sci.* **49**, 1494–1509 (1992).
29. L. C. Andrews et al., "Theory of optical scintillation," *J. Opt. Soc. Amer. A* **16**, 1417–1429 (1999).
30. L C. Andrews et al., "Theory of optical scintillation: Gaussian-beam wave model," *Waves Random Media* **11**, 271–291 (2001).
31. M. E. Gracheva and A. S. Gurvich, "Strong fluctuations in the intensity of light propagated through the atmosphere close to the Earth," *Soviet Radiophys.* **8**, 511–515 (1965).
32. K. S. Gochelashvili and V. I. Shishov, "Saturated fluctuations in the laser radiation intensity in a turbulent medium," *Sov. Phys. JETP* **39**(4), 605–609 (1974).
33. R. L. Fante, "Inner-scale size effect on the scintillations of light in the turbulent atmosphere," *J. Opt. Soc. Amer.* **73**, 277–281 (1983).
34. R. G. Frehlich, "Intensity covariance of a point source in a random medium with a Kolmogorov spectrum and an inner scale of turbulence," *J. Opt. Soc. Amer. A* **4**, 360–366 (1987); Errata "Intensity covariance of a point source in a random medium with a Kolmogorov spectrum and an inner scale of turbulence: Errata," J. Opt. Soc. Amer. A 4, 1324 (1987).
35. S. M. Flatté and J. S. Gerber, "Intensity-variance behavior by numerical simulation for plane-wave and spherical-wave optical propagation through strong turbulence," *J. Opt. Soc. Amer. A* **17**, 1092–1097 (2000).
36. D. L. Fried, "Aperture averaging of scintillation," *J. Opt. Soc. Amer.* **57**, 169–175 (1967).
37. E. L. Bass, B. D. Lackovic, and L. C. Andrews, "Aperture averaging of optical scintillations based on a spectrum with high wave number bump," *Opt. Eng.* **34**, 26–31 (1995).
38. J. H. Churnside, "Aperture averaging of optical scintillations in the turbulent atmosphere," *Appl. Opt.* **30**, 1982–1994 (1991).
39. A. Consortini et al., "Inner-scale effect on intensity variance measured for weak-to-strong atmospheric scintillation," *J. Opt. Soc. Amer. A* **10**, 2354–2362 (1993).
40. L. B. Stotts and L. C. Andrews, "Probability density function models for adaptive optical systems operating in turbulence," *Opt. Eng.* **63**(8), 088101 (2024).
41. L. C. Andrews, "Aperture-averaging factor for optical scintillations of plane and spherical waves in the atmosphere," *J. Opt. Soc. Amer. A* **9**, 597–600 (1992).
42. J. G Proakis, *Digital Communications*, 5th ed., McGraw-Hill, pp. 274–278 (2008).


**Larry B. Stotts** is a consultant. His interests are RF and optical communications, RF, infrared and visible surveillance, and reconnaissance. He received his BA degree in applied physics and

information sciences and his PhD in electrical engineering (communications systems), both from the University of California at San Diego. He has published over 117 journal articles and authored/co-authored four books. He is a fellow of the IEEE, the SPIE, and Optica.

**Larry C. Andrews** is a Professor Emeritus of Mathematics at the University of Central Florida (UCF) and an associate member of the Towns Laser Institute in the College of Optics/Center for Research in Electro-Optics and Lasers (CREOL) at UCF. He received his PhD in theoretical mechanics from Michigan State University. He has authored/coauthored 12 textbooks and has published numerous papers and reports. He is a fellow of the SPIE and authored three SPIE field guides.